International Journal of Heat and Fluid Flow 112 (2025) 109656

Contents lists available at ScienceDirect

International Journal of Heat and Fluid Flow

journal homepage: www.elsevier.com/locate/ijhff

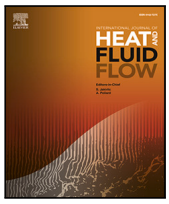

On the interaction of a laminar heated boundary layer with a roughness element: A comparison of experiments and simulations for steady flow

Frank G. Jacobitz [a,*], Ian Sysyn [a], Jacob Ryan [a], Jack Comfort [a], Patrick Bonner [a], Dylan Poole [a], Jonathan Lemarechal [b], Marco Costantini [b]

[a] Department of Mechanical Engineering, Shiley-Marcos School of Engineering, University of San Diego, 5998 Alcalá Park, San Diego, CA 92110, USA
[b] Deutsches Zentrum für Luft- und Raumfahrt, Bunsenstraße 10, 37073 Göttingen, Germany

ARTICLE INFO

Keywords:
Roughness element
Laminar boundary layer
Heated surface
Temperature-sensitive paint
Numerical simulation

ABSTRACT

The aim of this study is a direct comparison of experimental and simulation results of two flows, a laminar boundary layer developing on a flat heated plate and the interaction of a laminar boundary layer with a single cylindrical roughness element of small aspect ratio with a height similar to the boundary layer thickness. The experiments were performed in a water channel using temperature-sensitive paint (TSP) on a heated flat plate on which the boundary layer develops. The numerical simulations are meant to complement the experimental data, allowing for a direct comparison with the experiment and adding additional information not easily accessible from the experiment. In the case of the laminar boundary layer developing over a flat heated surface, experimental TSP measurements and simulation results of the surface temperature show strong agreement and a correlation coefficient for the two temperature fields of 0.99 is obtained. In the case of a laminar boundary layer interacting with a low aspect ratio roughness element, the comparison between experimental and numerical data revealed the role played by buoyancy effects even at the small implemented temperature differences between surface and fluid. With consideration of buoyancy in the simulations, again good agreement between the experimental and simulation results is obtained with a correlation coefficient of 0.95 for the respective temperature fields. The complex vortical system identified in the flow field via the simulations was shown to be consistent with the thermal footprints measured on the heated wall in the experiments.

1. Introduction

The flow over roughness elements is a fundamental problem in fluid mechanics and it has been extensively studied through experimental, numerical, and theoretical approaches. Research in this area has focused on understanding the impact of roughness elements on flow characteristics such as turbulence, separation, and transition. For practical uses, the research is motivated by the impact that roughness can have on the performance of aircraft, ships, re-entry vehicles, wind turbines, gas turbines, or other applications, where it can occur in the form of two-dimensional (*e.g.*, steps, gaps, or waviness), three-dimensional (*e.g.*, screw head slots, rivet heads, insect debris, or accumulation of dirt), and distributed roughness (*e.g.*, ice accretion, material erosion, or deteriorated surface coatings). Experimental studies have investigated different types of roughness configurations and their effects on flow over various geometries such as flat plates, cylinders, airfoils, and wings.

Experiments on three-dimensional roughness elements in laminar boundary layers have typically focused on the effect of the roughness on boundary-layer stability and transition to turbulence. The transition location is moved towards the roughness location very rapidly once a critical value of the roughness Reynolds number $Re_{kk} = u_k k/\nu_k$ (where k is height of the roughness, and u_k and ν_k are the flow velocity and kinematic viscosity at the wall-normal location corresponding to the roughness height, but in the absence of the roughness) has been exceeded, but that below this critical value an isolated three-dimensional element (subcritical roughness height) has little or no effect on the transition location (Klanfer and Owen, 1953; Klebanoff et al., 1955, 1992; Smith and Clutter, 1959; Tani et al., 1962; Braslow, 1960, 1966; Ergin and White, 2006; Plogmann et al., 2014). The critical value of the roughness Reynolds number $Re_{kk,cr}$ depends on several factors, including the shape factor of the roughness element (height-to-width ratio, see Smith and Clutter, 1959; Braslow, 1960, 1966).

* Corresponding author.
E-mail address: jacobitz@sandiego.edu (F.G. Jacobitz).

https://doi.org/10.1016/j.ijheatfluidflow.2024.109656
Received 23 December 2023; Received in revised form 7 November 2024; Accepted 8 November 2024
Available online 12 December 2024

The flow topology about an isolated three-dimensional roughness element in a laminar boundary layer at sufficiently high values of Re_{kk} (but still below the critical roughness Reynolds number) consists mainly of: a steady horseshoe vortex, which wraps around the upstream side of the roughness element and trails two steady counter-rotating legs downstream, and a closely spaced pair of vortex filaments, which form in the near wake, rise vertically and trail downstream once they reach the level of the top of the roughness element (Gregory and Walker, 1956; Tani et al., 1962; Klebanoff et al., 1992). The wake of a roughness element may be characterized by a complex interaction of vortical structures and flow instabilities, which may eventually lead to transition to turbulence. The discussion of this complex flow evolution is not a purpose of this introduction; the reader is therefore referred to the given references (see Gregory and Walker, 1956; Tani et al., 1962; Acarlar and Smith, 1987; Klebanoff et al., 1992; White and Reshotko, 2002; Ergin and White, 2006; Plogmann et al., 2014, among others). Furthermore, a recent review of the impact of roughness in turbulent flows is provided by Chung et al. (2021).

A wide variety of measurement techniques have been applied in the investigation of the flow field around a single three-dimensional roughness element and to study the influence of three-dimensional roughness elements on the laminar to turbulent boundary layer transition. Besides velocity measurement techniques such as Particle Image Velocimetry (PIV) (Ye et al., 2016) and Lagrangian particle tracking (Schröder et al., 2020), surface based flow visualization techniques like thermographic methods, *e.g.*, Thermochromic Liquid Crystals (TLC) (Clark et al., 1993; Zhong et al., 2003), InfraRed Thermography (IRT) (Avallone et al., 2016; Zoppini et al., 2022), and the Temperature-Sensitive Paint (TSP) method (Fey et al., 2003; Costantini et al., 2015; Lemarechal et al., 2020; Miozzi et al., 2024) have been applied to investigate the occurring phenomena.

The TSP method is an optical, non-intrusive measurement technique, which measures surface temperatures based on the temperature-dependent fluorescence of specialized surface coatings. As summarized in Liu et al. (2021), the TSP method has numerous applications in fluid dynamics research, including boundary-layer transition studies and heat-transfer analysis. In contrast to IRT, the TSP method is well suited for water applications (Fey et al., 2013; Capone et al., 2015; Lemarechal et al., 2021), since the involved wave lengths range from near-UV to red light.

The use of thermographic measurement techniques for boundary layer investigations relies on the temperature changes induced over the exposed surface by different boundary layer states (laminar-turbulent transition, see, *e.g.*, Fey et al., 2003; Fey and Egami, 2007; Costantini et al., 2015, 2021) or flow structures within the boundary layer (footprints of coherent structures, see, *e.g.* Fey and Egami, 2007; Lemarechal et al., 2020, 2019a,b, 2021; Miozzi et al., 2024). At low Reynolds numbers and/or in incompressible flows, the temperature variations caused by the flow structures over an adiabatic wall (less than 0.1 K) are too small for being detected via thermographic measurement techniques (Fey and Egami, 2007). Thus, an artificial heat flux is utilized to enhance the flow-induced temperature variations. Depending on fluid, flow speed, flow field and orientation of the flat plate in the gravitational field, buoyancy forces can be excited. Thus, the imposed heat flux must be small enough to avoid significant buoyancy effects, which would lead to a deviation of the actual flow field from that at adiabatic-wall conditions. For example, Lemarechal et al. (2018) observed that buoyancy effects led to the prevention of laminar re-attachment of a separation bubble, which was caused by a forward–backward facing step at low flow speeds in a water facility.

The present work focuses on the application of TSP in water to examine subcritical roughness conditions as investigated in Lemarechal et al. (2020) (roughness Reynolds number $Re_{kk} = 355$), for which the wake was reported to remain laminar. An isolated three-dimensional (cylindrical) roughness element in a two-dimensional laminar boundary layer at low Reynolds numbers is investigated experimentally and numerically. The laminar boundary layer develops on a flat plate, which is heated after a long unheated starting length. For this flow configuration the literature provides only few results, which mainly describe the onset of mixed convection and associated vortical structures (Miller et al., 2018). Earlier studies did not discuss the onset of buoyancy effects, which is however relevant to evaluate whether the introduced heat flux still enables a non-intrusive TSP measurement.

This work has three goals. First, experimental and simulation results of the steady flow in the absence and in the presence of the cylindrical roughness element are compared, focusing on the identification of the heat flux effectively transferred from the heating layer below the TSP to the fluid domain. Second, the three-dimensional flow structure induced by the roughness element is described using the simulation results, thus allowing the interpretation of the thermal signatures at the wall observed in the TSP results. Finally, the influence of the heat flux of the TSP measurement on the flow is investigated by comparing numerical data with and without buoyancy effects and the experimental results.

In the following, the experimental and simulation approaches are introduced. Then, experimental and simulation results are presented, discussed, and compared. Finally, the observations are summarized and an outlook on future work is provided.

2. Experimental and numerical simulation approach

In this section, the experimental setup and the simulation approach are briefly described. The goal of both, the experiment and the simulation, is the study of the interaction of a zero-pressure-gradient Blasius boundary layer with a roughness element. However, due to the finite water depth in the experiment and a finite domain size in the simulation, a slight favorable pressure gradient is present in both studies. A coordinate system with x in the streamwise direction, y in the wall-normal direction, and z in the spanwise direction is used.

2.1. Experimental methods

2.1.1. Temperature-Sensitive Paint method

A TSP coating for water applications consists of a clear coat with embedded luminescent molecules (called luminophores), which is applied onto the surface of interest. The luminophores are excited by light of an appropriate wave length; the return to the ground state occurs predominantly by one of two processes: emission of light (fluorescence) or radiationless (thermal quenching). The intensity of the emitted light, which has a larger wave length than the excitation light (Stokes shift), decreases with a higher temperature. The emitted light can be detected by means of a photosensitive device, such as Charge-Coupled Device (CCD) and Complementary Metal-Oxide Semiconductor (CMOS) cameras, thus enabling the non-intrusive, global measurement of the temperature distribution on the surface of an object, even with high temporal and spatial resolution. Further details on TSP working principle and characteristics, paint formulations, data evaluation techniques and measurement applications are provided in Liu et al. (2021).

The first application of the TSP method in water flows were quantitative flow visualizations of a cylinder in cross-flow (Fey et al., 2013). These visualizations clearly demonstrated the TSP capabilities for achieving time-resolved information on near-wall fluid structures. Afterwards, further tests investigated the laminar separation bubble and the turbulent separation of the cylinder in cross-flow for a larger range of Reynolds numbers (Capone et al., 2015; Miozzi et al., 2016). A second geometry considered for fundamental research is the Blasius boundary layer flow over a flat plate at nearly-zero pressure gradient, which has been studied via TSP in the presence of two-dimensional and three-dimensional roughness (Lemarechal et al., 2018, 2020), for K-type transition (Lemarechal et al., 2019b), and in the presence of pronounced buoyancy effects (Mäteling et al., 2020). More practical

applications are the investigations of a NACA 0015 hydrofoil: isolated in cross-flow (Miozzi et al., 2019) as well as in the wake of a marine propeller (Miozzi and Costantini, 2021); those investigations also enabled the analysis of the flow topology and of the intermittent events occurring in the separated flow regions. All these experiments demonstrated the capability of TSP to provide time-resolved measurements of unsteady flow phenomena over large areas, which is favorable due to the reduced characteristic frequencies in water facilities. These conditions even enable sophisticated data evaluation to determine the skin friction (Miozzi et al., 2019; Lemarechal et al., 2021; Miozzi et al., 2024).

2.1.2. Experimental setup

The experiment investigating a laminar boundary layer over a heated surface without and with a cylindrical roughness element was conducted in the laminar water channel (Laminarwasserkanal, Strunz and Speth, 1987) of the Institute of Aerodynamics and Gas Dynamics at the University of Stuttgart. In this facility, a laminar boundary layer flow develops over a flat plate of 8 m length and 1.2 m width at a distance of 0.15 m to the free water surface. The velocity range in the laminar water channel is 0.04 m/s to 0.2 m/s and a low turbulence level (below 0.05 % in the relevant frequency range of 0.1 Hz to 10 Hz) is characteristic for the flow (Wiegand, 1996; Puckert et al., 2017).

The roughness element has a height of $k = 0.01$ m and a diameter of $D = 0.03$ m, which results in an aspect ratio of $D/k = 3$. Note that this ratio is significantly larger than those investigated in other studies focusing on cantilevered circular cylinders (see Sumner et al., 2004; Morton et al., 2018, among others), where $D/k \leq 0.5$. For the comparison with the numerical work only the position of the roughness element $x_k = 0.57$ m from the leading edge of the momentum boundary layer is considered. The freestream velocity examined in the present work is $U = 0.04$ m/s, as determined at the position of the roughness element x_k. The roughness Reynolds number of the test case is $Re_{kk} = 355$, with the required velocity u_k analytically determined from the Blasius flow at the wall-normal location corresponding to the upper edge of the roughness element.

Measurements with TSP are conducted in the laminar water channel with a thin plate made of fiber reinforced plastics, which is mounted on the flat plate and provides a substrate for the TSP coating and the electrical model heating. As discussed in Section 1, the latter is necessary for the enhancement of the surface temperature differences induced by the flow structures. The TSP element mounted on the flat plate has a total size of $x \times z = 1.07$ m $\times$ 1.00 m and its leading edge is positioned 0.53 m downstream of the leading edge of the flat plate. On the TSP element, an area of $x \times z = 1.00$ m $\times$ 0.25 m is coated with a TSP based on an Europium complex (Ondrus et al., 2015). The integrated model heating is composed of two patches of a current-carrying layer of carbon fiber with an area of $x \times z = 0.50$ m $\times$ 0.30 m, which are arranged in flow direction with a gap of 0.02 m. The beginning of the heated area is at approximately $x = 0.55$ m, *i.e.*, the heating starts about 0.005 m upstream of the front side of the roughness element. A detailed description of the TSP element is provided by Lemarechal et al. (2019b).

The TSP data acquisition is made in a top-view setup through the free water surface. As shown in Fig. 1, two *HARDsoft IL-105/6X Illuminator* Light-Emitting Diodes (LEDs) and a monochromatic *pco.4000* 14-bit scientific CCD camera are used to excite the luminophores and acquire the light emitted by the TSP, respectively. The optical setup provides a resolution of approximately 2.8 pixels/mm for a field of view of $x \times z = 0.7$ m $\times$ 0.25 m. The TSP data were acquired at a frequency of 10 Hz.

The TSP data acquisition procedure is segmented into a reference phase and a run phase. In the reference phase, TSP images are acquired at a temperature equilibrium of fluid and TSP surface to record the reference luminescent intensity distribution I_{ref} at a known reference temperature T_{ref}. Afterwards, the electrical heating is started with a

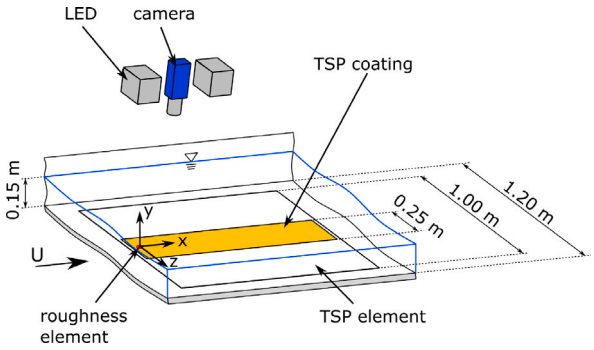

Fig. 1. Schematic of the experimental setup.

constant electrical power of 40 W, *i.e.*, at an electrical power density of 133.3 W/m^2. The applied heat flux was assumed in Mäteling et al. (2020) to be low enough to avoid buoyancy effects on the examined boundary layer development; however, as reported later in the present work, buoyancy effects were indeed appreciable in the presence of a roughness element, even at the investigated, relatively low roughness Reynolds number $Re_{kk} = 355$.

When the TSP surface temperature is increased by approximately 1 K above T_{ref}, the run phase is started. During the run phase, 40 images of luminescent intensity distribution are acquired with a constant heat flux. Please note that, while the electrical power density provided to the heating layer patches is known, its fraction transferred into the liquid region is not known. One motivation of the present study is to determine the heat flux density provided to the liquid domain through the comparison between experimental and numerical results.

The TSP data reduction comprises of averaging the images acquired in reference phase, the division of the averaged reference images and each run image, and a projection of the resulting images onto a structured grid representing the TSP element surface (mapping). Thus, a time series of intensity-ratio maps was generated in physical space. This latter operation is performed by means of the DLR software package *ToPas* (Klein et al., 2005), relying on the known positions of fiducial markers in the TSP coating. Finally, the intensity-ratio maps are converted to temperature maps by applying a simplified empirical relation

$$T - T_{ref} = \frac{1}{S} \ln \frac{I_{ref}}{I} \tag{1}$$

for each grid point (Liu et al., 2021). The temperature sensitivity S is obtained from a calibration of a TSP sample coated simultaneously to the model; the calibration is conducted in a dedicated calibration chamber under controlled conditions (Egami et al., 2009). Finally, each temperature map of the time series is filtered with a median filter (5 mm $\times$ 5 mm) before deriving the temporal average and standard deviation.

Several aspects contribute to the uncertainty of the temperature measurement with TSP, including uncertainty of the reference temperature measurement, calibration uncertainty, relative motion between model and camera system, changes in the optical path, uncertainty of the intensity measurement, and uncertainty of the illumination (Liu et al., 1995; Cattafesta et al., 1998). The experimental setup of Lemarechal et al. (2021) utilized the same camera, LEDs, and TSP coating. The reported uncertainty of the temperature measurement with TSP ($\Delta T \approx 0.3$ K) is therefore also considered in the present work. Similarly, the uncertainty of the free-stream velocity is estimated to be $\Delta U = \pm 0.0012$ m/s) as in Lemarechal et al. (2021). The uncertainty of the reference temperature, which is assumed to be equal to the fluid temperature, is estimated to be $\Delta T_0 = \pm 0.5$ K in the current paper.

Table 1
Relationship between the different origin locations for the x-coordinate. The corresponding streamwise coordinates are given for coordinate systems with origins at the inflow plane, leading edge of the momentum boundary layer (BL), leading edge of the thermal boundary layer, and roughness element (RE) center are shown.

	Inflow	Momentum BL	Thermal BL	RE Center	Outflow
Inflow	0 m	0.4 m	0.94 m	0.97 m	1.45 m
Momentum BL	−0.4 m	0 m	0.54 m	0.57 m	1.05 m
Thermal BL	−0.94 m	−0.54 m	0 m	0.03 m	0.51 m
RE Center	−0.97 m	−0.57 m	−0.03 m	0 m	0.48 m

Further information on the experimental setup as well as on the TSP data analysis for a larger range of roughness Reynolds numbers is provided by Lemarechal et al. (2020).

2.2. Simulation approach

The simulations are performed using the ANSYS Fluent computational fluid dynamics (CFD) software package. It is widely used to simulate fluid flow and heat transfer in a broad range of engineering applications. It is part of the ANSYS suite of simulation tools and is widely used in industries such as aerospace, automotive, chemical, energy, and biomedical engineering (ANSYS, Inc, 2023).

This study is based on the steady incompressible Navier–Stokes equations and an advection/diffusion equation for the temperature. Simulations excluding and including buoyancy effects are performed. In the cases without buoyancy effects, the fluid density is constant and determined from the inflow temperature. In the cases with buoyancy, the Boussinesq approximation is used, which neglects density differences in the inertia terms, but considers the density differences in the body force term due to the acceleration of gravity. This approach is valid for flows involving small temperature differences as they are present in the flows considered here.

The computational domain consists of three subdomains as shown in Fig. 2 for the case of a laminar boundary layer developing over a heated flat plate and in Fig. 3 for the case of the interaction of a laminar boundary layer with a low aspect ratio roughness element.

Upstream of the leading edge of the flat plate, the inflow is allowed to develop in a $L_x \times L_y \times L_z = 0.4\ \text{m} \times 0.1\ \text{m} \times 0.2\ \text{m}$ subdomain with a symmetry boundary condition at $y = 0$ in the y-direction. This symmetry boundary conditions allows the flow to slow upstream of the leading edge to obtain a better agreement with the experimental results. Starting from the leading edge, a laminar boundary layer forms in an unheated $0.54\,\text{m} \times 0.1\,\text{m} \times 0.20\,\text{m}$ subdomain. This is followed by a heated $0.51\,\text{m} \times 0.1\,\text{m} \times 0.2\,\text{m}$ subdomain. The roughness element is placed $0.03\,\text{m}$ downstream from the start of the heated subdomain, which corresponds to a distance of $0.57\,\text{m}$ from the leading edge of the flat plate or $0.97\,\text{m}$ from the start of the symmetry boundary condition subdomain (see also Table 1). Please note that the start of the heated region is moved upstream by a distance of $0.01\,\text{m}$ as compared to the experiment. This change was required in order to match the experimental results, as it captures the effects of inhomogeneous heating and horizontal conduction upstream in the plate (see discussion in Section 3.1). Additionally, a zero gauge pressure is specified at the outlet plane. The no-slip condition is imposed on the flat plate at $y = 0$ in the unheated and heated subdomains. The top and sides of the domains use no-stress boundary conditions.

Different coordinate systems with the origin of the x-coordinate at the inflow plane, leading edge of the momentum boundary layer, leading edge of the thermal boundary layer, and center location of the roughness element are used. The relationships between the different coordinate systems are shown in Table 1. The solid plate surface is located at $y = 0$ and the centerline in the cross-stream direction is located at $z = 0$.

Figs. 2 and 3 also show the temperature evolution on the surface ($y = 0$) based on simulation data without buoyancy effects. In the symmetry boundary condition subdomain and the unheated subdomain, the temperature remains constant and at the value of the inflow temperature of $T_0 = 291.22\,\text{K}$ and $T_0 = 291.72\,\text{K}$ for the boundary layer and roughness element simulations, respectively. In the heated subdomain, the temperature increases in the streamwise direction. The results will be discussed in detail in Section 3.

For the simulation of a laminar boundary layer over a heated plate, the computational grid used within the Fluent meshing software was a Cartesian-based mesh with a total of 18,075,321 mesh elements and 18,413,517 nodes. The symmetry, non-heated, and heated subdomains contained 1,000,000, 3,287,900, and 13,787,421 mesh elements as well as 1,035,351, 3,379,062, and 13,999,104 mesh nodes, respectively. The mesh for the symmetry subdomain did not have a bias and used a Cartesian mesh with the element size of $0.002\,\text{m}$. The non-heated subdomain had a Cartesian-based mesh with a base element size of $0.002\,\text{m}$ and an edge sizing bias on all 4 edges along the x-direction. This bias resulted in a higher mesh density towards the interfaces between the subdomains. This bias type was accomplished using 490 divisions and a bias factor of 8 in the Fluent software. Finally, the heated subdomain did not have a bias and used a Cartesian mesh with an element size of $0.001\,\text{m}$.

For the simulation of a laminar heated boundary layer interacting with a roughness element, the computational grid used within the Fluent meshing software was adopted to the presence of the roughness element. In this case, the Cartesian-based mesh had a total of 18,065,949 mesh elements and 18,404,849 nodes. The mesh geometries for the symmetry and non-heated subdomains remained unchanged. The heated subdomain contained 13,778,049 mesh elements and 13,990,436 mesh nodes, resulting in a similar resolution to the case without a roughness element decribed above. Its Cartesian-based mesh with a base element size of $0.001\,\text{m}$ did not have a bias and blended around the surface of the roughness element. A grid convergence study was performed in order to assure that the chosen grid resolution is sufficient.

An inlet velocity $U = 0.0377\,\text{m/s}$ is specified at the inflow plane. Due to the finite size of the computational domain of $0.1\,\text{m}$ in the vertical direction, the mass flow deficit in the boundary layer results in an increase of the freestream velocity far away from the wall (mass conservation). The resulting acceleration corresponds to a small favorable pressure gradient. This effect could be avoided with a substantially larger computational domain in the vertical direction, but, with fixed computational resources available, only at the expense of resolution in the boundary layer region.

Therefore, the inlet velocity was adjusted to match the freestream velocity of the experiment ($U = 0.04\,\text{m/s}$) at a location $0.57\,\text{m}$ downstream from the leading edge of the momentum boundary layer, *i.e.*, the location of the roughness element. At a location $0.57\,\text{m}$ downstream from the leading edge of the momentum boundary layer, *i.e.*, the location of the roughness element, a freestream velocity of about $U = 0.04\,\text{m/s}$ is obtained, which matches the freestream velocity of the experiment.

3. Results and discussion

In this section, the evolution of two flows is discussed based on a comparison of experimental and simulation results. First, the evolution of a laminar boundary layer over a flat heated plate is presented. Second, the interaction of a laminar boundary layer with a low aspect ratio roughness element is discussed. In both cases, simulations without and with a consideration of buoyancy effects are performed. Finally, the three-dimensional vortical structures in the flow's interior, as obtained from the simulations, are related to their thermal footprints, as observed by the experiment through the use of TSP.

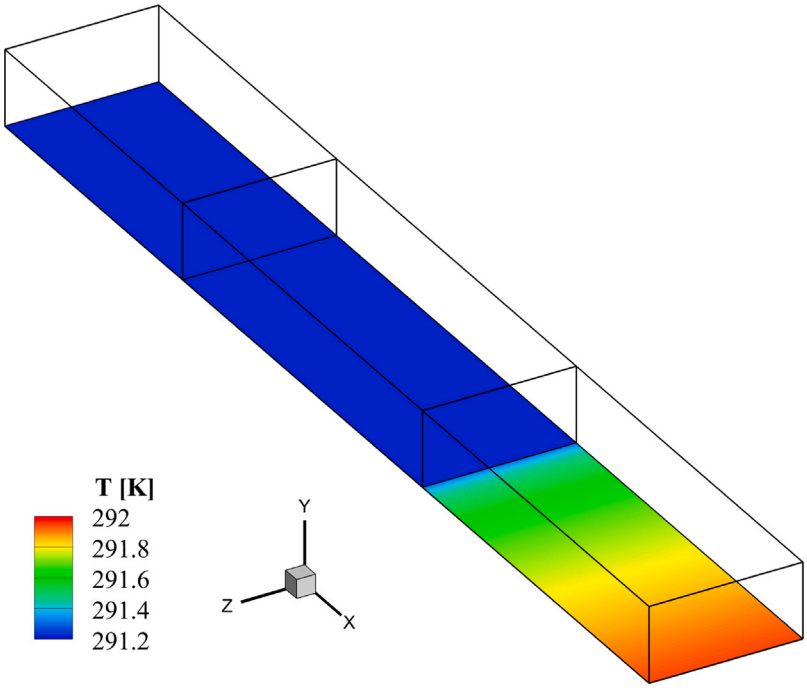

Fig. 2. Schematic of the computational domain for the simulation of a laminar boundary layer over a heated surface. The temperature distribution obtained from the simulation on the bottom surface of the computational domain is shown for clarity (case without buoyancy effects). The schematic shows the three subdomains: upstream of the leading edge using a symmetry boundary condition at $y = 0$, the unheated domain over a flat plate with a no-slip boundary condition at $y = 0$, and a heated domain over a flat plate with a no-slip boundary condition and an imposed constant heat flux density at $y = 0$.

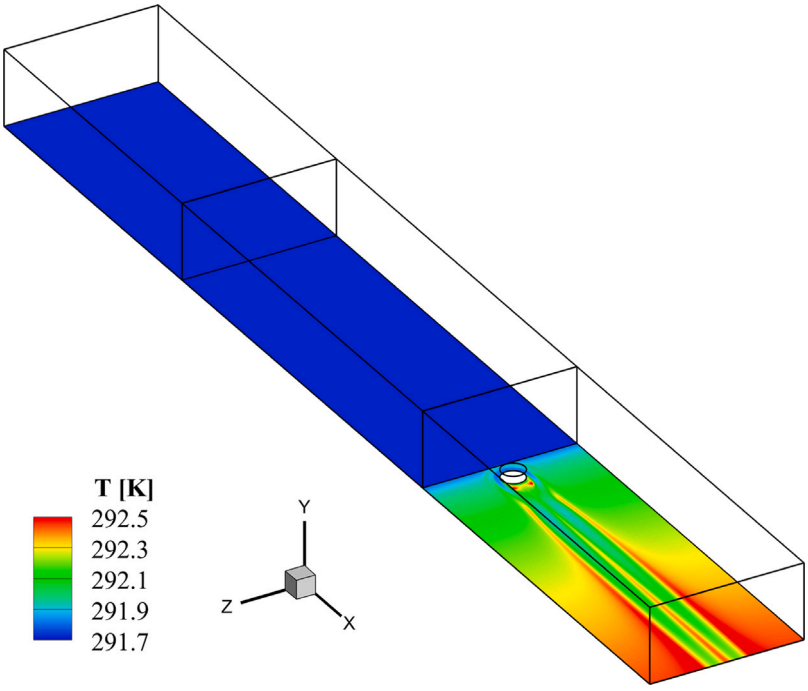

Fig. 3. Schematic of the computational domain for the simulation of the interaction of a laminar boundary layer with a roughness element. The temperature distribution obtained from the simulation on the bottom surface of the computational domain is shown for clarity (case without buoyancy effects). The schematic shows the three subdomains: upstream of the leading edge using a symmetry boundary condition at $y = 0$, the unheated domain over a flat plate with a no-slip boundary condition at $y = 0$, and a heated domain over a flat plate with a no-slip boundary condition and an imposed constant heat flux density at $y = 0$. Additionally, the location of the roughness element is indicated in the figure.

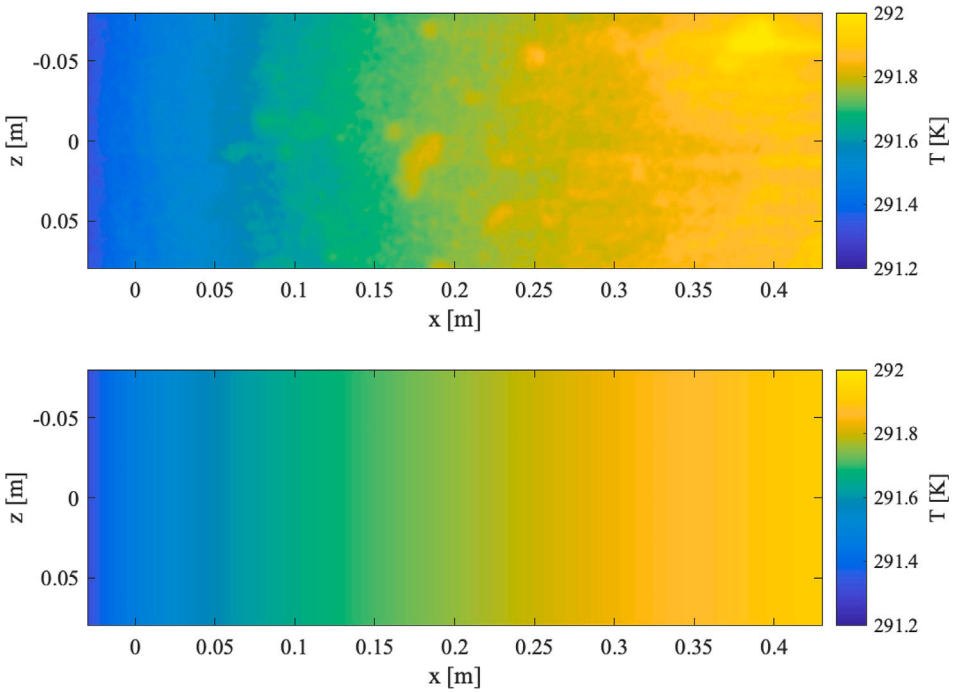

Fig. 4. Surface temperature in the heated region from the experiment (top) and the simulation (bottom). The origin with $x = z = 0$ corresponds to the center position of the roughness element (not present here) to enable a better comparison with Fig. 10 (see also "RE Center" reference system in Table 1.

3.1. Laminar boundary layer over a flat heated plate

The experimental case of a laminar boundary layer developing over a flat heated plate has a freestream velocity of $U = 0.04\,\mathrm{m/s}$ (determined 0.57 m downstream of the leading edge), an inlet temperature of $T_0 = 18.3\,^\circ\mathrm{C} = 291.45\,\mathrm{K}$, and a heat flux density of $133.3\,\mathrm{W/m^2}$ supplied to the heated plate. The boundary layer first develops for 0.55 m over an unheated flat plate, followed by a further 0.5 m of flow over a heated plate. The TSP region starts at 0.53 m, or 0.02 m upstream from the heated region.

Fig. 4 (top) shows the surface temperature of the heated region as determined from the TSP observation. For comparison purposes, the $x = 0$ location coincides with the location of the center of the roughness element, which is not present in this case. This corresponds to the "RE Center" reference system in Table 1. Hence, the temperature development is shown 0.01 m past the start of the TSP region and 0.01 m upstream of the start of the heated region. A temperature increase is already visible upstream of the heated region, which is likely due to upstream horizontal heat conduction in the plate.

The temperature increases in the streamwise direction from its inflow value. There is a slight temperature variation for a given streamwise location in the cross-stream direction, which is partially due to the low-level velocity fluctuations in the water channel (turbulence level (below 0.05 %), and partially apparent (*i.e.* due to measurement noise). However, this temperature variation is less than $\pm 0.05\,\mathrm{K}$.

The simulated case of a laminar boundary layer developing over a flat heated plate has an inlet velocity of $U = 0.037\,\mathrm{m/s}$, an inlet temperature of $T = 18.07\,^\circ\mathrm{C} = 291.22\,\mathrm{K}$, and a heating power density of $100\,\mathrm{W/m^2}$. The simulation is performed with a constant density and, hence, without the consideration of buoyancy effects. The boundary layer first develops for 0.54 m over an unheated flat plate, which is 0.01 m less than for the experiment, followed by a further 0.51 m of flow over a heated plate. Temperature information is available at any location in the simulation domain. The chosen inlet temperature in the simulation of 291.22 K is slightly lower than that of the experiment of 291.45 K, but within the experimental uncertainty. It was adjusted to match the experimental temperature evolution, as discussed below.

A summary of parameters obtained from the simulation of a laminar boundary layer of a heated plate without buoyancy effects is given in Table 2. The displacement thickness $\delta_1 = \int_0^\infty (1 - u/U)\,dy$, the momentum thickness $\delta_2 = \int_0^\infty u/U(1 - u/U)\,dy$, the shape factor $H = \delta_1/\delta_2$, the thermal displacement thickness $\beta_1 = \int_0^\infty \Theta\,dy$, and the local freestream velocity U are given for locations $x = 0.57\,\mathrm{m}$ and $x = 1\,\mathrm{m}$ from the leading edge of the momentum layer. Here, $x = 0.57\,\mathrm{m}$ corresponds to the location of the roughness element (not present in this case) and $x = 1\,\mathrm{m}$ is close to the outflow plane of the simulation domain. The nondimensional temperature is defined as $\Theta = (T - T_0)/(T_S - T_0)$, where T_0 is the freestream temperature of the water and T_S the surface temperature of the heated plate at a given streamwise location.

At the eventual location of the roughness element with height $k = 0.01\,\mathrm{m}$, the Reynolds numbers $Re_k = Uk/\nu$ and $Re_{kk} = u_k k/\nu$ are determined, where U is the freestream velocity and u_k is the velocity in the laminar boundary layer at the height of the roughness element, *i.e.*, at $y = 0.01\,\mathrm{m}$. The values of the Reynolds numbers Re_k and Re_{kk} obtained for the simulations (see Table 2) are slightly different from those provided for the experiments (Lemarechal et al., 2020). The discrepancy is due to a slightly different value for the viscosities (due to slightly different inflow temperatures) and slightly different velocities (estimated from Blasius flow in the experiment, but determined from the simulation data in the simulation case).

Fig. 4 (bottom) shows the surface temperature of the heated region as determined from the Fluent simulation (see Section 2.2). As introduced above, an upstream shift by 0.01 m of the heated region as compared to the experiment was required in order to obtain comparable results and to account for horizontal, upstream conduction of heat in the plate not captured in the simulation. The surface temperature obtained from the simulation increases in the streamwise direction and it compares well with the experiment. The correlation coefficient of the surface temperature fields obtained from experiment and simulation was determined to be 0.99, being the correlation missing to reach a coefficient of 1 mainly due to the slight cross-stream variations in the experiment. The correlation coefficient between the surface temperatures determined by the experiment and simulation was computed by

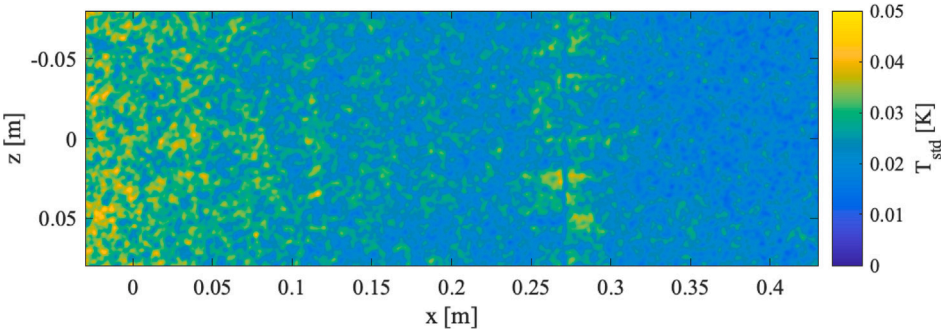

Fig. 5. Temporal standard deviation of the surface temperature in the heated region from the experiment. The origin with $x = z = 0$ corresponds to the center position of the roughness element (not present here).

Table 2
Parameters obtained from the simulation of a laminar boundary layer over a heated plate at two locations $x = 0.57$ m (location of the center of the roughness element not present here) and $x = 1$ m (close to outflow plane) in the "Momentum BL" reference system (see Table 1).

x	0.57 m	1.00 m
δ_1	0.0060 m	0.0077 m
δ_2	0.0024 m	0.0031 m
H	2.52	2.50
β_1	0.0011 m	0.0027 m
U	0.0401 m/s	0.0409 m/s
Re_k	399	
u_k	0.0327 m/s	
Re_{kk}	326	

mapping the results onto a common grid. The correlation coefficient between two variables x and y over a two-dimensional area A is then determined as $\sum_A (x_i - \bar{x})(y_i - \bar{y}) / \sqrt{\sum_A (x_i - \bar{x})^2} \sqrt{\sum_A (y_i - \bar{y})^2}$. Here $\bar{x}$ denotes the average of the variable x computed on the area A.

Fig. 5 shows the standard deviation of the fluctuations of the surface temperature as determined from the 20 temperature maps. As can be seen, the distribution of the temperature standard deviation is smaller than the uncertainty reported in Section 2.1.2 for the whole examined domain. Nevertheless, a vertical stripe of slightly higher standard deviation can be observed between $x = 0.25$ m and 0.3 m. This was likely due to the camera characteristics, since it requires image read out via two analog-to-digital converters to achieve the acquisition frequency of 10 Hz. The minuscule differences of the analog-to-digital converters are enhanced when the images are mapped onto the surface grid leading to the visible stripe in Fig. 5.

The simulation of a laminar boundary layer developing over a flat heated plate was repeated and buoyancy effects were included using a thermal expansion coefficient of $\beta = 2.07 \times 10^{-4}\ \mathrm{K}^{-1}$ and the Boussinesq model was used to represent buoyancy forces in the Navier–Stokes equations. The results were found to be essentially identical to the case without the consideration of buoyancy effects, which is now discussed further.

A direct comparison of the streamwise temperature evolution as observed by the experiment and the simulation is shown in Fig. 6. The streamwise distribution of the average temperature value T_e and the spatial standard deviation σ_{T_e} is obtained by computing a cross-stream average and standard deviation of the measured TSP surface temperatures. This is compared to the streamwise temperature T_s obtained by the simulation. As there is no temperature variation in the cross-stream direction in the simulation, the centerline value at $z = 0$ is used. At all streamwise locations, the temperature value obtained by the simulation T_s falls within the $T_e - \sigma_{T_e}$ to $T_e + \sigma_{T_e}$ interval. The temperature increase observed in the experiment starting 0.01 m upstream from the location of the heated region, indicates the presence of horizontal conduction in the upstream direction and justifies that the simulations start the heated region 0.01 m upstream from the experiment. Similarly, the average temperature drop observed at the downstream end of the heated region is likely also due to streamwise horizontal conduction, effectively lowering the heat addition to the fluid interior and decreasing the temperature.

Data as shown in Fig. 6 was used to determine the combination of inlet temperature $T = 18.07\,^{\circ}\mathrm{C} = 291.22\,\mathrm{K}$ and heat flux density of $100\,\mathrm{W/m^2}$ as the best fit to the experimentally measured temperature evolution over the heated section of the flat plate. For the purpose of matching the simulation results to the experimental data, a number of different simulations were performed at different inflow temperatures and heat flux densities. A linear interpolation of the results was used to determine the approximately best match with the experimental data. This was followed by small adjustments of the inflow temperature by 0.01 K, until the best agreement with the experimental temperature evolution was obtained. During this matching procedure, it became clear that good agreement could only be obtained by starting the heated region in the simulations 0.01 m upstream from the location of the heated region in the experiment, in order to account for horizontal conduction in the plate in the upstream direction. It should be emphasized here that the matched simulation enabled a quantification of the loss of electrical heating power density in the experiment, which was known to occur due to losses in the electrical wiring and in the heat transfer away from the water region, but could not yet be quantified.

In the following, some additional simulation results of the laminar boundary layer case are presented, which are not available from the experiment. Fig. 7 shows the normalized vertical velocity profiles and their comparison with the Blasius solution at distances of 0.2 m, 0.4 m, 0.6 m, 0.8 m, and 1.0 m downstream of the leading edge of the momentum boundary layer. Following classical Blasius boundary layer scaling, the vertical axis is scaled as $\eta = y\sqrt{U/(\nu x)}$ and the streamwise velocity in the boundary layer profile is scaled with its freestream value as u/U.

The upstream-most velocity profile at 0.2 m from the leading edge agrees well with the Blasius solution. The small favorable pressure gradient (see Section 2.2) leads to the slightly fuller velocity profiles, as compared to the Blasius solution, observed further downstream from the leading edge. This observation is consistent with a shape factor value $H = \delta_1/\delta_2 = 2.50$ close to the outlet plane in the simulation domain at $x = 1$ m. A similar acceleration is also present in the experiment due to the finite depth of the water layer over the plate. The experiments are performed with a water depth of 0.15 m over the plate and report a 3 % deviation of the shape factor from its classical value for a zero-pressure-gradient Blasius boundary, corresponding to a value of about 2.51 (Wiegand, 1996).

Vertical profiles of normalized temperature are shown in Fig. 8 at locations 0.26 m, 0.36 m, and 0.46 m downstream of the leading edge of the thermal boundary layer or 0.8 m, 0.9 m, and 1.0 m downstream of the leading edge of the momentum boundary layer. The vertical axis is again normalized as $\eta = y\sqrt{U/(\nu x)}$. Generally, a good collapse

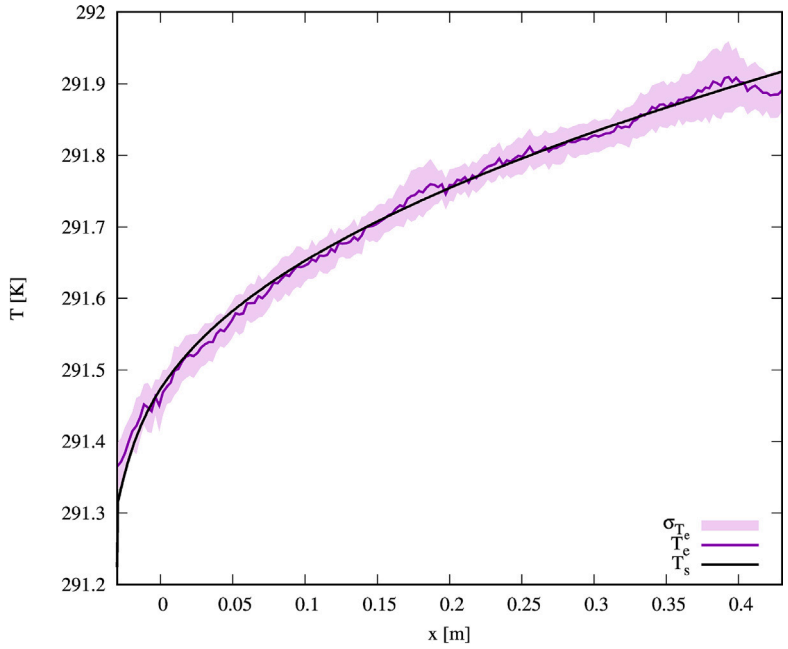

Fig. 6. Streamwise temperature evolution. The experimentally measured surface temperature is averaged in the cross-stream direction and the resulting streamwise average temperature profile T_e and standard deviation σ_{T_e} are shown. Additionally, the surface temperature from the simulation T_s is shown for comparison. The origin with $x = 0$ corresponds to the center position of the roughness element (not present here) to enable a better comparison with Fig. 4.

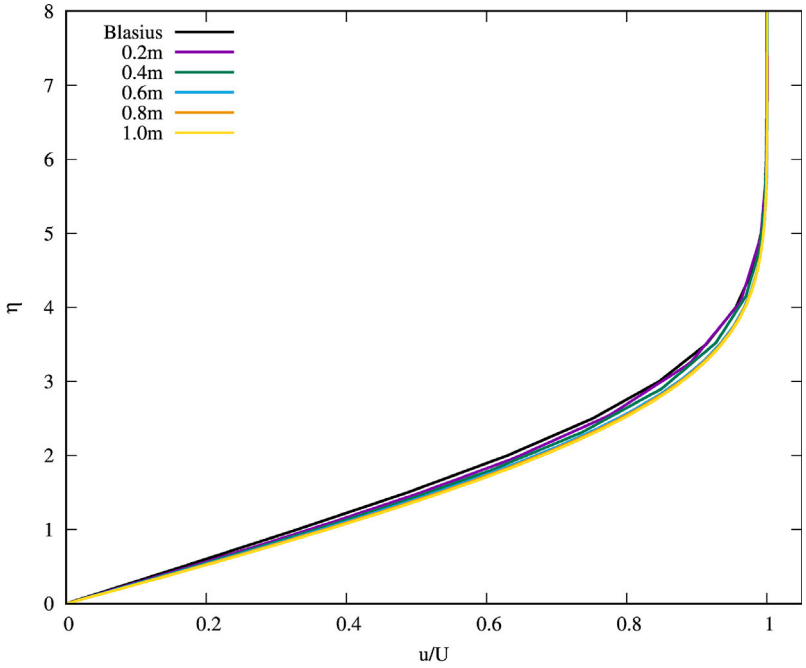

Fig. 7. Normalized vertical velocity profiles of η vs. u/U and comparison to the Blasius solution. The streamwise distance given is measured from the leading edge of the momentum boundary layer, which starts 0.4 m from the inlet plane of the simulation (see Table 1).

of the normalized temperature profiles is obtained. However, just as the normalized velocity profiles in Fig. 7, the normalized temperature profiles in Fig. 8 become fuller in the more downstream locations due to the weak favorable pressure gradient present in the simulations.

Lastly, the wall shear stress τ_W is shown for the heated region in Fig. 9. As expected, the wall shear stress decreases in the streamwise direction. From the wall shear stress on the heated surface, a drag force $F_D = 0.366 \times 10^{-3}$ N was computed.

3.2. Heated laminar boundary layer with a low aspect ratio roughness element

The experimental case of a heated laminar boundary layer interacting with a low aspect ratio roughness element was generally performed under the same conditions as the case without a roughness element. The center of the roughness element of diameter 0.03 m and height 0.01 m was placed on the plate at a streamwise location of 0.57 m from the leading edge of the momentum boundary layer or 0.02 m downstream from the leading edge of the heated section. The inlet velocity of U

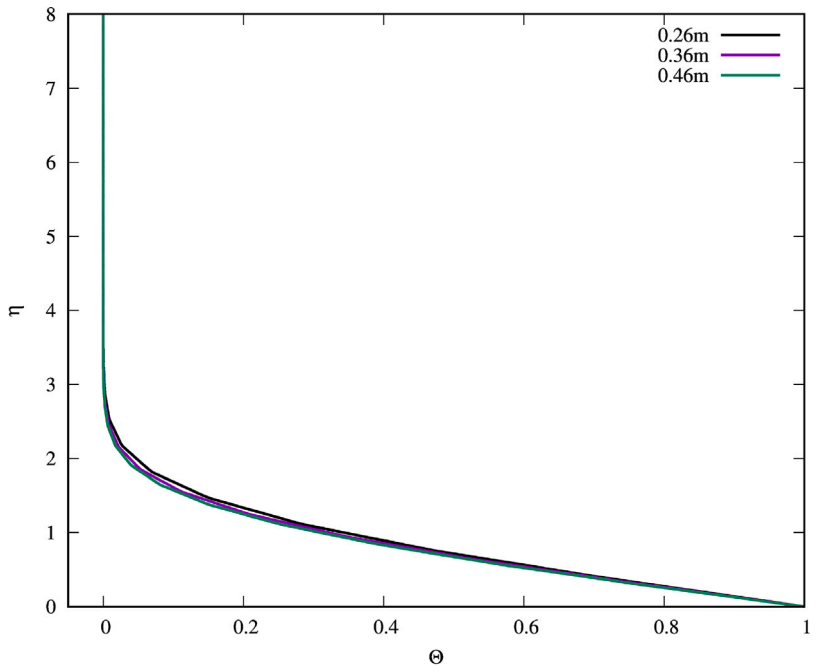

Fig. 8. Normalized vertical temperature profiles of η vs. Θ. The streamwise distance given is measured from the leading edge of the thermal boundary layer, which starts 0.54 m from the leading edge of the momentum boundary layer or 0.94 m from the inlet plane of the simulation (see Table 1).

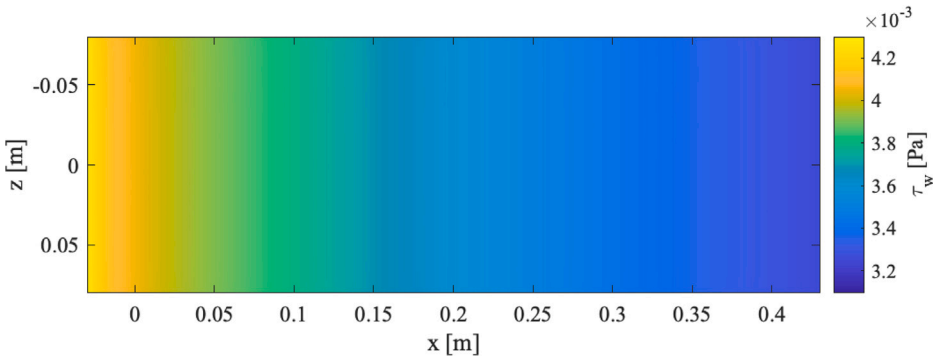

Fig. 9. Wall shear stress in the heated region from the simulation. The origin with $x = z = 0$ corresponds to the center position of the roughness element (not present here) to enable a better comparison with Fig. 13.

= 0.04 m/s and a total electrical heating power of $Q = 40$ W remained unchanged. Due to the continuous heat addition into the water channel during experimental runs, the inlet temperature was likely higher than the original value of $T_0 = 18.3\,°\text{C} = 291.45\,\text{K}$, but it remained within the reported uncertainty interval for the temperature measurement.

Fig. 10 (top) shows the surface temperature in the heated region as obtained from the TSP measurement. Away from the roughness element and its wake, a temperature increase in the streamwise direction is observed, which is similar to the temperature increase of the case without a roughness element. Just upstream of the roughness element, a region of low temperature is observed. This low temperature is partially due to the entrainment of colder water at the inlet temperature as induced by a horseshoe vortex around the upstream half of the roughness element. The temperature, however, is somewhat further lowered due to the shade of the roughness element in the TSP measurement (lightpath from the LEDs to the surface). In the near wake downstream of the roughness element, a fairly stagnant recirculation zone is visible, which is at a somewhat elevated temperature due to reduced heat transport away from this region. In the wake of the roughness element, a temperature signature due to the presence of counter-rotating vortex pairs extending downstream from the roughness element is visible. Downward transport of water at the inlet temperature cools the heated plate along the two streamwise-oriented stripes, while an elevated temperature is observed in the centerline region and on the cross-stream boundaries of the wake region. The surface temperature distribution is consistent with the topology reported in previous work in the presence of cylindrical roughness elements (see Gregory and Walker, 1956; Tani et al., 1962; Klebanoff et al., 1992; Plogmann et al., 2014; Ye et al., 2016, among others), being the result of the transport of cold/warm water via coherent structures (horseshoe vortex and counter-rotating vortex pairs). These flow structures were already shown to induce low and high speed streaks in earlier work, and the current investigation additionally shows their thermal impact on a heated surface.

Fig. 11 shows the temporal standard deviation of the surface temperature as determined from the 40 experimental temperature maps. Again, the standard deviation was smaller than the reported experimental uncertainty. Nevertheless, a vertical stripe of slightly larger standard deviation, similar to that observed in Fig. 5, can again be seen in this figure. The largest values of standard deviation are found in the close vicinity of the roughness element, because of the impact of the shading and of the low signal-to-noise ratio discussed above. The three horizontal stripes of slightly larger standard deviation visible

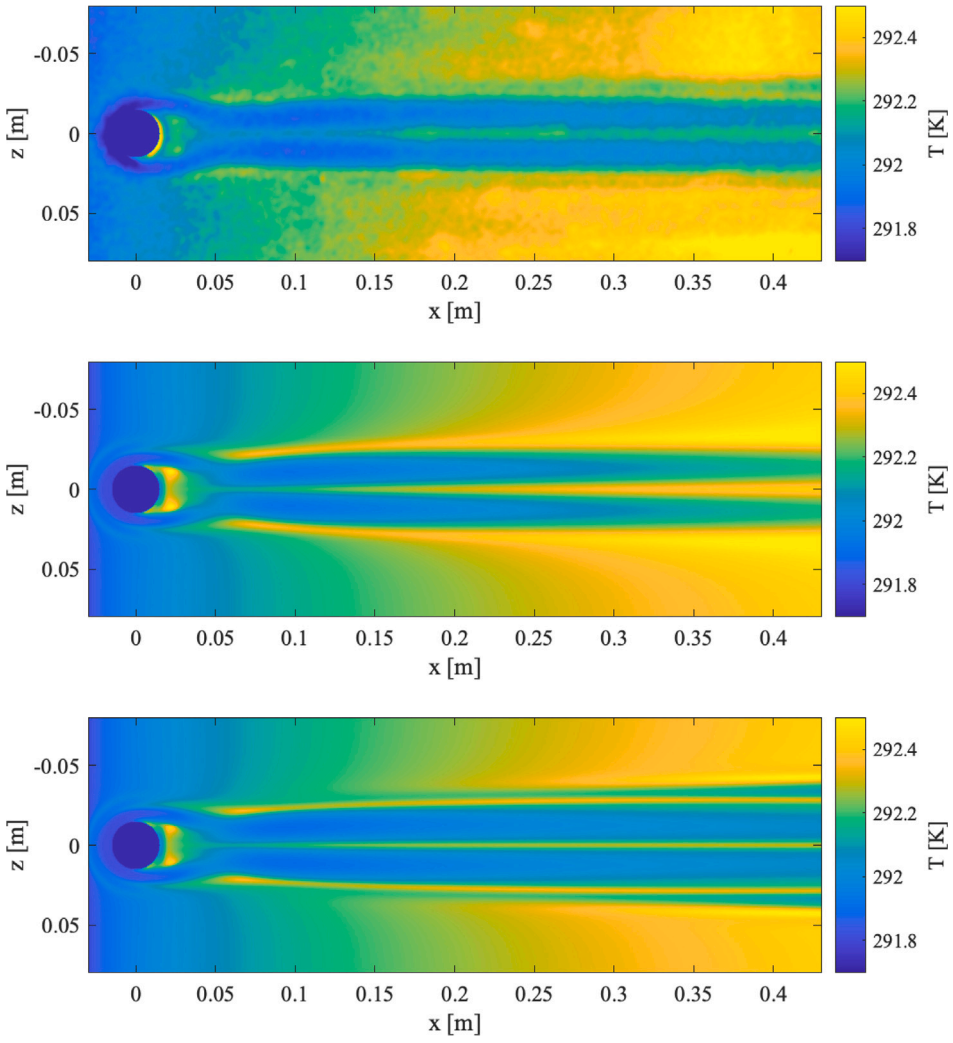

Fig. 10. Surface temperature in the heated region from the experiment (top), the simulation excluding buoyancy effects (center), and the simulation including buoyancy effects (bottom). The origin with $x = z = 0$ corresponds to the center position of the roughness element.

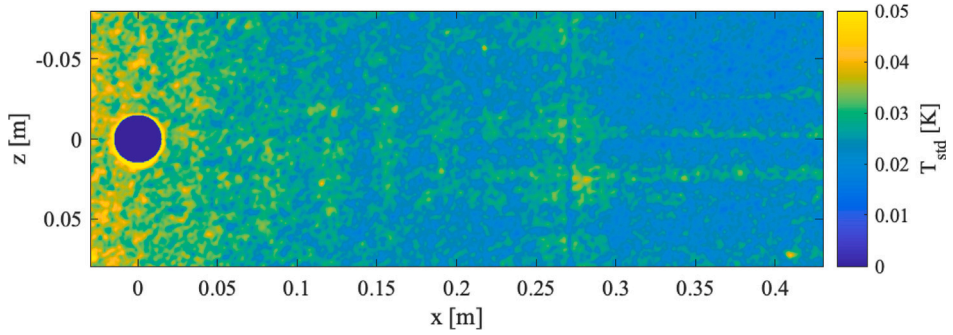

Fig. 11. Temporal standard deviation of the surface temperature in the heated region from the experiment. The origin with $x = z = 0$ corresponds to the center position of the roughness element.

at approximately $x > 0.25\,\mathrm{m}$ were likely due to slight fluctuations in position and strength of the vortical structures in the wake of the roughness element.

The simulated case of a laminar boundary layer interacting with a low aspect ratio roughness element was also performed under similar conditions as the case without a roughness element, but with an adjusted freestream temperature. The inflow temperature to obtain agreement was selected as $T_0 = 18.57\,^{\circ}\mathrm{C} = 291.72\,\mathrm{K}$. This higher temperature likely reflects a higher water temperature in the experiment after multiple experimental runs, but it also falls within the uncertainty interval of the freestream temperature measurement. It should also be emphasized here that the adjustment procedure of the freestream

temperature aimed to match the experimental temperature evolution in the region at $z \leq -0.05\,\mathrm{m}$, *i.e.*, away from the roughness element and its wake.

The surface temperature in the heated region as obtained from the Fluent simulation with a constant density and thus excluding buoyancy effects is shown in Fig. 10 (center). The simulation generally captures the elements of the experimentally observed temperature field. There is also a relatively cold region just upstream of the roughness element, a warmer recirculation zone in the near wake just downstream of the roughness element, two cooled regions due to the counter-rotating vortex pairs in the wake, and warmer temperatures in the centerline region and in the cross-flow boundaries of the wake. The temperature signature obtained by the simulation is generally more pronounced than the distribution obtained in the experiment. The correlation coefficient of the experimental and simulated surface temperature fields is 0.90, indicating a first, fair agreement of the temperature signatures of the relatively complex near and far wake structures between experiment and simulation.

A closer evaluation of the differences between the surface temperature fields obtained experimentally and from this constant density simulation excluding buoyancy effects reveals two colder surface structures that are visible in the experimental temperature data, but they are absent in the simulation results. These structures form approximately at the end of the near wake structure at a downstream position $x = 0.1\,\mathrm{m}$ and they border the outer edges of the surface temperature signatures of the two counter-rotating vortex pairs in the wake of the roughness element. In the downstream area of the wake around $x = 0.4\,\mathrm{m}$, the colder structures are visible approximately at cross-stream locations $z = \pm 0.03\,\mathrm{m}$ (see Fig. 10, top). These band structures of colder surface temperatures are absent in the surface temperature fields obtained from the simulation without buoyancy effects (see Fig. 10, center).

In order to understand the origin of the colder temperature bands observed in the experimental data, the Fluent simulation was repeated with buoyancy effects included. Again, a thermal expansion coefficient of $\beta = 2.07 \times 10^{-4}\,\mathrm{K}^{-1}$ was used in conjunction with a Boussinesq model to represent buoyancy forces in the Navier–Stokes equations. The surface temperature in the heated region as obtained from the Fluent simulation including buoyancy effects is shown in Fig. 10 (bottom). The surface temperature field shows, in general, the same topology as that discussed with regard to the case without buoyancy effects, but with additional colder stripes at cross-flow boundaries of the wake.

These stripes of colder surface temperatures originate from a location suitable for the onset of buoyancy effects due to the lower flow velocities in the near wake structure combined with higher surface temperatures at that location. They resemble the action of tertiary and further counter-rotating vortex pairs, such as those described in Ye et al. (2016), which may be indeed triggered by buoyancy. In fact, two further stripes of higher temperature are observed in the simulation with buoyancy effects at approximately $x > 0.25$ m at the cross-stream boundaries of the additional colder stripes; they are consistent with the further vortex pairs emerging in these regions, as will be discussed below.

The buoyancy-induced heat transfer away from and towards the heated plate results in stripes of lower/higher surface temperature. The correlation coefficient of the experimental and simulated surface temperature fields is increased to 0.95 with buoyancy effects considered in the simulation. This indicates an improved agreement of the temperature signatures of the relatively complex near and far wake structures and the low temperature bands bordering the wake structure. The main reasons for a correlation coefficient slightly different from one are the factors affecting the experimental data in the vicinity of the roughness element, which were discussed above.

The correlation between experimental and numerical results with buoyancy effects included is analyzed in more detail by comparing surface temperature profiles extracted in the cross-stream direction at four streamwise locations: $x = 0\,\mathrm{m}$, $0.03\,\mathrm{m}$, $0.15\,\mathrm{m}$, and $0.30\,\mathrm{m}$ in the "RE Center" reference system. These locations correspond to the roughness element center, the near wake, and two locations in the far wake, allowing for the discussion of its development. The comparison is presented in Fig. 12. At the roughness element location (top figure), the temperature profiles are qualitatively in agreement, with the minima and maxima of the surface temperatures induced by the action of the horseshoe vortex observed at essentially the same cross-stream locations.

Nevertheless, the magnitude of these temperature variations is weaker in the experimental results, as compared to the numerical data. This is likely due to a combination of the aforementioned shade of the roughness element in the TSP measurement and of the different heat conduction in the vicinity of the roughness element, which was made of brass. This latter influence was analogous to that discussed in Miozzi et al. (2024) for a wall-mounted cube. At larger cross-stream distances from the roughness element, at $z \leq -0.05\,\mathrm{m}$, the temperature values are in agreement, as achieved through the adjustment procedure in the simulations to match the experimental streamwise evolution of the temperature in this region (see above). On the other side, at $z \geq 0.05\,\mathrm{m}$, the temperature from the experimental results was slightly larger than that in the simulations. This small asymmetry in the experimental data (less than $0.1\,\mathrm{K}$) was probably due to manufacturing tolerances in the layers composing the TSP element. Away from the centerline, the matched temperature values at $z < 0\,\mathrm{m}$ and the remaining temperature difference $z > 0\,\mathrm{m}$ are obviously observed also downstream of the roughness element, as can be seen in Fig. 12.

In the near wake, at $x = 0.03\,\mathrm{m}$, the agreement of experimental and numerical results is remarkable at $z < 0\,\mathrm{m}$, with the minima and maxima of the surface temperatures at essentially the same cross-stream locations, and only slight differences in the temperature values up to $z \approx -0.04\,\mathrm{m}$. At $z > 0\,\mathrm{m}$, minima and maxima of the surface temperature appear to be slightly shifted towards larger z-values, as compared to the numerical data, likely because of the aforementioned manufacturing effects of the TSP element.

In the far wake, at $x = 0.15\,\mathrm{m}$, the agreement of the temperature profiles is nearly excellent for the main low-temperature stripes, *i.e.*, between $z \approx \pm\,0.005\,\mathrm{m}$ and $z \approx \pm\,0.025\,\mathrm{m}$. The local temperature maxima at $z = 0\,\mathrm{m}$ and $z \approx \pm\,0.025\,\mathrm{m}$ are slightly lower in the experimental results than in the numerical data, probably because of cross-stream heat conduction in the TSP element that was not accounted for in the simulations. The situation is similar further downstream, at $x = 0.30\,\mathrm{m}$. Remarkable agreement is observed for the main low-temperature stripes, whereas cross-stream heat conduction likely influenced the temperature maximum at $z = 0\,\mathrm{m}$ and the temperature distribution at $|z| \gtrapprox 0.02\,\mathrm{m}$: in these two latter regions more distant from the centerline, local minima and maxima in the experimental results appear to be "smeared" and slightly shifted in the cross-stream direction towards $z = 0\,\mathrm{m}$, as compared to results of the numerical simulations without in-plane heat conduction.

Based on the comparison of the experimentally determined surface temperature fields with those obtained from simulations excluding and including buoyancy effects, we conclude that buoyant motions were present in the experiment on the laminar boundary layer interacting with a roughness element. It is common practice to use the Richardson number to identify the impact of natural convection in a certain flow. However, in the present case of a roughness element in a laminar boundary layer, multiple choices for the reference length in the Richardson number are possible. When using the streamwise coordinate x (*e.g.*, Bird et al., 2002), Richardson numbers between approximately 0 and 1 are found in the heated domain. This would be a range of Richardson numbers in which natural convection may play a role. Nevertheless, it should be noted here that the Richardson numbers for the case without roughness element would be in the same range, and no buoyancy effects were observed. It may therefore be inferred for the present case that an additional flow modulation induced by the roughness element was needed to "trigger" buoyancy

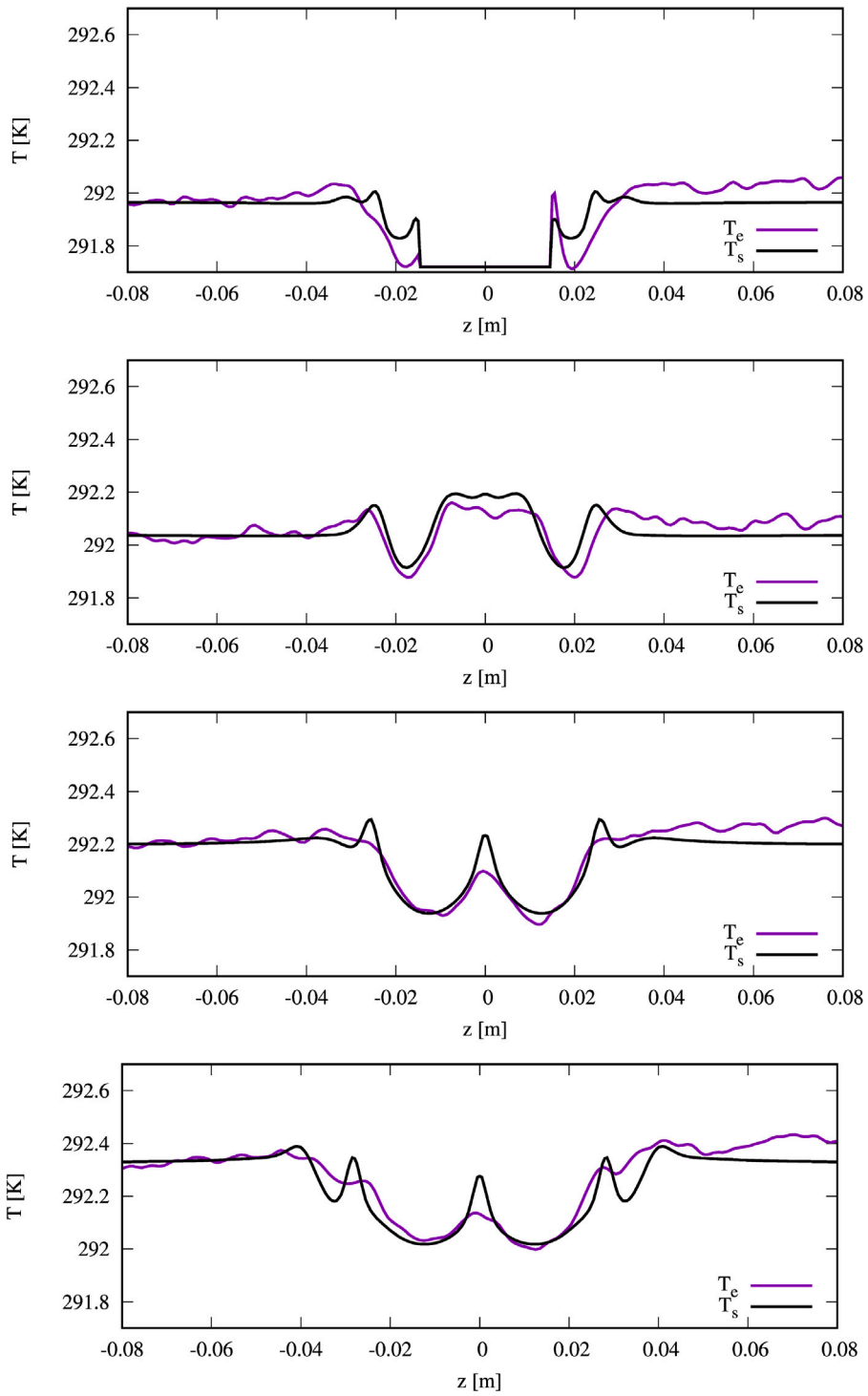

Fig. 12. Comparison of the temperature profiles obtained by experiment T_e and simulation T_s in the cross-stream direction z at $x = 0\,\mathrm{m}$ ($x = x_k$), $0.03\,\mathrm{m}$ ($x/k = 1$), $0.15\,\mathrm{m}$ ($x/k = 5$), and $0.30\,\mathrm{m}$ ($x/k = 10$) from the center of the roughness element. The origin with $x = z = 0$ corresponds to the center position of the roughness element.

effects. Although this inference may not be generalizable for other flows, the conclusion of the current analysis would be that care is needed when Richardson numbers above about 0.1 are expected. In such cases, it is recommended to reduce the temperature difference between model surface and flow as much as possible to avoid buoyancy effects. These findings should be considered in future experiments using thermographic methods in water flows, especially when regions of reduced flow velocity (such as in the presence of two-dimensional or three-dimensional roughness, or in the case of an adverse pressure gradient due to, *e.g.*, the curvature of a hydrofoil) are expected. At larger flow speeds (and therefore Reynolds numbers), buoyancy effects would be expected to be negligible with the current temperature differences, even in the presence of a roughness element.

The wall shear stress distribution over the heated region is shown in Fig. 13. The top of the figure shows the results from the simulation excluding buoyancy effects and the bottom of the figure shows the corresponding result from the simulation including buoyancy results. In both cases, a region with strong wall shear stress is observed just upstream of the roughness element in the formation region of the horseshoe vortex. The near wake region shows the transition of the

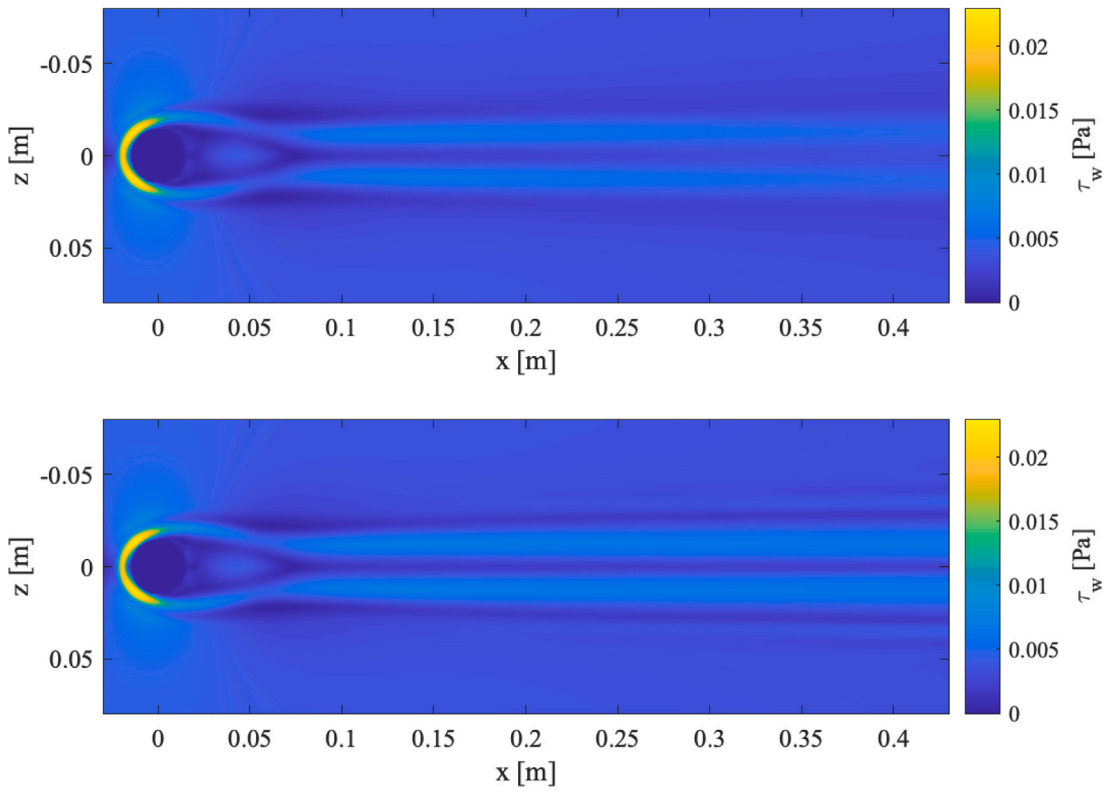

Fig. 13. Wall shear stress in the heated region from the simulation excluding buoyancy (top) and including buoyancy (bottom). The origin with $x = z = 0$ corresponds to the center position of the roughness element.

horseshoe vortex into a counter-rotating vortex trail in the far wake (see also the graphical abstract) as well as the location of the vortex pair forming just behind the roughness element. The results from the simulation including buoyancy effects additionally shows bands of lower and higher wall shear stress bordering the signatures of the main counter-rotating vortex pair in the wake of the roughness element. These bands are consistent with the surface temperature maps presented in Fig. 10 (bottom), as expected from the relation between wall shear stress and heat flux. Generally, the wall shear stress is of a similar magnitude as in the case without a roughness element. Using the heated surface, roughness element top surface, and roughness element sides, a total drag force $F_D = 0.415 \times 10^{-3}$ N was computed for the case excluding buoyancy effects. The additional bands of lower temperature and higher wall shear stress observed in the case including buoyancy effects result in a higher total drag force $F_D = 0.435 \times 10^{-3}$ N. These values are larger than that obtained for the laminar boundary layer simulation without a roughness element ($F_D = 0.366 \times 10^{-3}$ N), clearly showing the impact of the roughness element on the total drag force.

3.2.1. Flow field results from the numerical simulations

In the following, the three-dimensional flow structure in the vicinity of the roughness element as well as its wake is discussed using slices of streamwise velocity, temperature, and Q-criterion values in planes normal to the streamwise direction at the four locations $x = 0\,\text{m}$, $0.03\,\text{m}$, $0.15\,\text{m}$, and $0.30\,\text{m}$ in the "RE Center" reference system that were already considered in Fig. 12 with regard to the cross-stream surface temperature profiles. The Q-criterion is defined as $Q = 1/2(\|\Omega\|^2 - \|S\|^2)$, where S and Ω are the symmetric and antisymmetric components of the velocity gradient tensor, respectively. S is the rate of strain tensor and Ω the vorticity tensor. The results presented here are complemented by multimedia files of the streamwise velocity, temperature, and Q-criterion visualizations in planes normal to the streamwise direction. As time progresses in the movies, the streamwise position advances from $-0.025\,\text{m}$, corresponding to a position just upstream of the roughness element, to $0.45\,\text{m}$, corresponding to a position in the far wake close to the outflow plane. Fig. 14 shows slices of streamwise velocity at the roughness element and in its wake. Away from the centerline location for $|z| \geq 0.06\,\text{m}$, the thickness of the laminar boundary layer and its streamwise growth is visible. At the location of the roughness element with $x = 0\,\text{m}$, the boundary layer thickness is of similar height as the roughness element as intended by the design of the experiment and the matching simulations. The slice also shows the location of the horseshoe vortex wrapping around the roughness element, resulting in larger velocity adjacent to the plate and close to the roughness element at $z = \pm 0.02\,\text{m}$, complemented by lower velocity adjacent to the plate at about $z = \pm 0.025\,\text{m}$. In the near wake with $x = 0.03\,\text{m}$, the recirculation zone past the roughness element is characterized by low streamwise velocity. The location of the vortex pair originating from the horseshoe vortex is also visible, having the locations of these vortical structures slightly moved away from the centerline. The further evolution of the wake and the vortex pair is clarified by the slices in the wake at $x = 0.15\,\text{m}$ and $x = 0.30\,\text{m}$. While the boundary layer thickness continues to increase, the vortex pair moves outward and decreases in strength. Comparing the cases excluding (left column) and including (right column) buoyancy effects, the flow around the roughness element and in the near wake remains fairly unaffected. In the far wake, the location of the main counter-rotating vortex pair is more pronounced in the case including buoyancy effects. The main low- and high-speed streaks presented in Fig. 14 are in agreement with those reported in previous work on cylindrical roughness elements with large D/k (see Gregory and Walker, 1956; Tani et al., 1962; Klebanoff et al., 1992; Plogmann et al., 2014; Ye et al., 2016, among others).

Fig. 15 presents slices of temperature across the roughness element and in its wake. As for the momentum boundary layer, the development of the thermal boundary layer is visible away from the centerline and wake for $|z| \geq 0.06\,\text{m}$. The temperature of the water close to

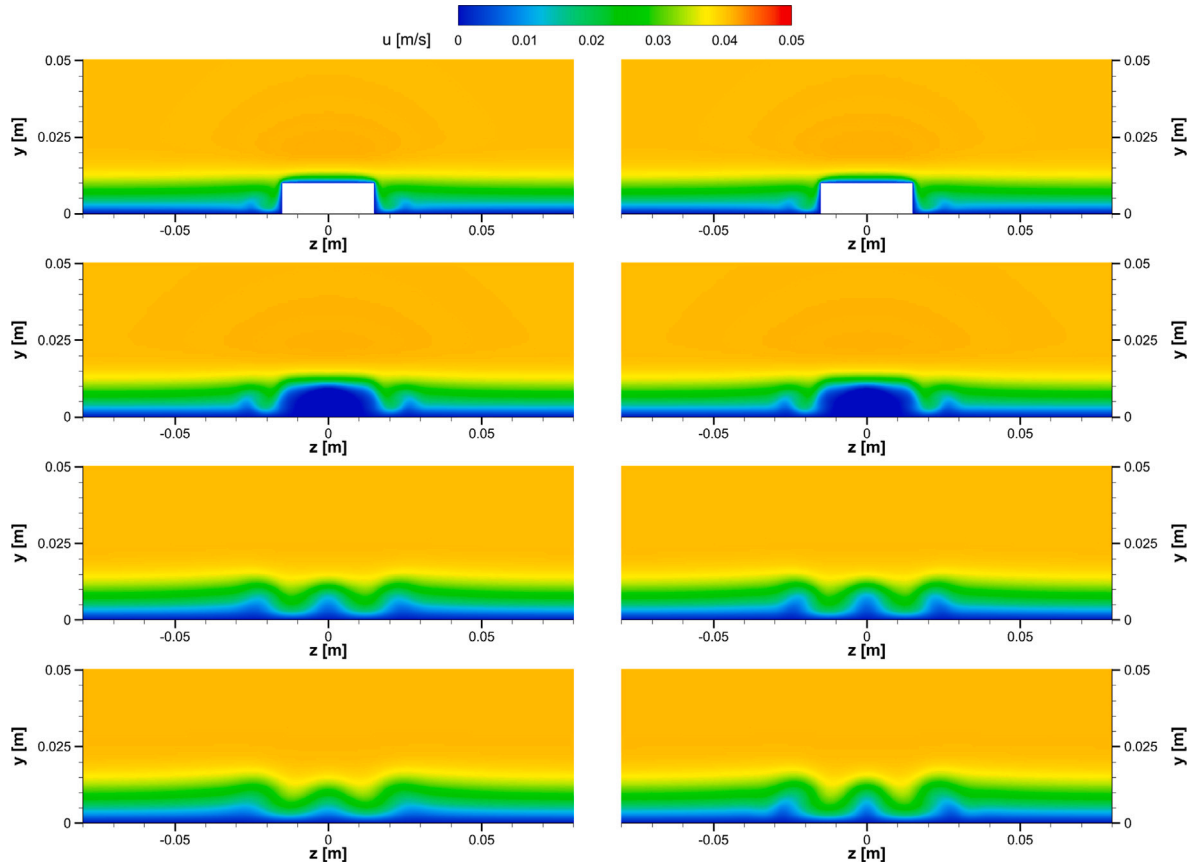

Fig. 14. Cross sectional view of the streamwise velocity component at $x = 0\,\mathrm{m}$ ($x = x_k$), $0.03\,\mathrm{m}$ ($x/k = 1$), $0.15\,\mathrm{m}$ ($x/k = 5$), and $0.30\,\mathrm{m}$ ($x/k = 10$) from the center of the roughness element. The origin with $x = z = 0$ corresponds to the center position of the roughness element. The left and right columns show results for simulations excluding and including buoyancy effects, respectively.

the surface continues to increase due to the constant heat flux into the liquid domain for the heated region. As expected from classical boundary layer scaling with $\delta_\Theta \sim \delta_u Pr^{-1/2}$, the thermal boundary layer is substantially thinner as compared to the momentum boundary layer. It still shows the features of the horseshoe vortex developing around the roughness element, which pushes colder water down towards the plate, resulting in colder water in the regions close to the roughness element, and it also pulls warmer water up further away from them. In the near wake, the recirculation zone shows an accumulation of warmer water, which is consistent with an observation of higher surface temperatures (see Fig. 10) and lower streamwise velocity (see Fig. 14). Further downstream in the wake region at $x = 0.15\,\mathrm{m}$ and $x = 0.30\,\mathrm{m}$, the outward spreading away from the centerline and decay of the main vortex pair strength is evident in the temperature signature. Comparing the cases excluding (left column) and including (right column) buoyancy effects, the temperature increase in the near wake at $0.03\,\mathrm{m}$ is reduced for the case including buoyancy effects. In the far wake, the location of the main counter-rotating vortex pair is again more pronounced in the case including buoyancy effects.

The three-dimensional structure of the horseshoe vortex, its development in the near wake, and the evolution of the counter-rotating vortex pairs in the far wake are even more clearly visualized with the help of the Q-criterion in Fig. 16. In the cross-section through the roughness element at $x = 0$, a complex structure of velocity gradients is visible. The strongest gradients are observed very close to the roughness element side and top surfaces, with a maximum close to its upper edges (intersection of side and top surfaces). These locations of large values of the Q-criterion are also observed on the upstream side surface and top surface (see graphical abstract). The cross-section also shows the development of the strong horseshoe vortex, which wraps around the front of the roughness element, borders the near wake region, and interconnects to the trailing vortex pair. A little further away from the roughness element and closer to the plate, a secondary horseshoe vortex, also wrapping around the roughness element, is revealed by the simulation. The thermal signature of this secondary vortical structure at the wall was likely too weak to be clearly distinguished in the temperature distribution measured in the experiment with the available signal-to-noise ratio upstream of the roughness element, as it can be barely seen in the surface distributions of temperature and shear stress in the simulations. Its thermal impact on the surface may be also further weakened by the in-plane heat conduction and by the (low-level) disturbances in the laminar water channel.

In the near wake region, at $x = 0.03\,\mathrm{m}$ in the "RE Center" reference system, strong gradients exist along the streamwise and vertical interface between the recirculation zone and the developing trailing vortices. Higher gradients also persist above the recirculation zone at the approximate height of the roughness element. Additionally, the slice also shows the locations of the counter-rotating trailing vortices. Their further development in the wake is shown at $x = 0.15\,\mathrm{m}$ and $x = 0.30\,\mathrm{m}$, as already discussed above with respect to Figs. 14 and 15. Comparing the cases excluding (left column) and including (right column) buoyancy effects, the vortex structures around the roughness element and in the near wake again remain fairly unaffected. At $x = 0.15$ m, the tertiary vortex pair discussed above is clearly identified in the case including buoyancy effects. In the far wake, a more pronounced and more complex system of vortical structures can be seen at $x = 0.30\,\mathrm{m}$ when buoyancy effects are considered. The further vortical structures are here identified via the Q-criterion, thus substantiating the wall signatures previously discussed with regard to Figs. 10 and 13.

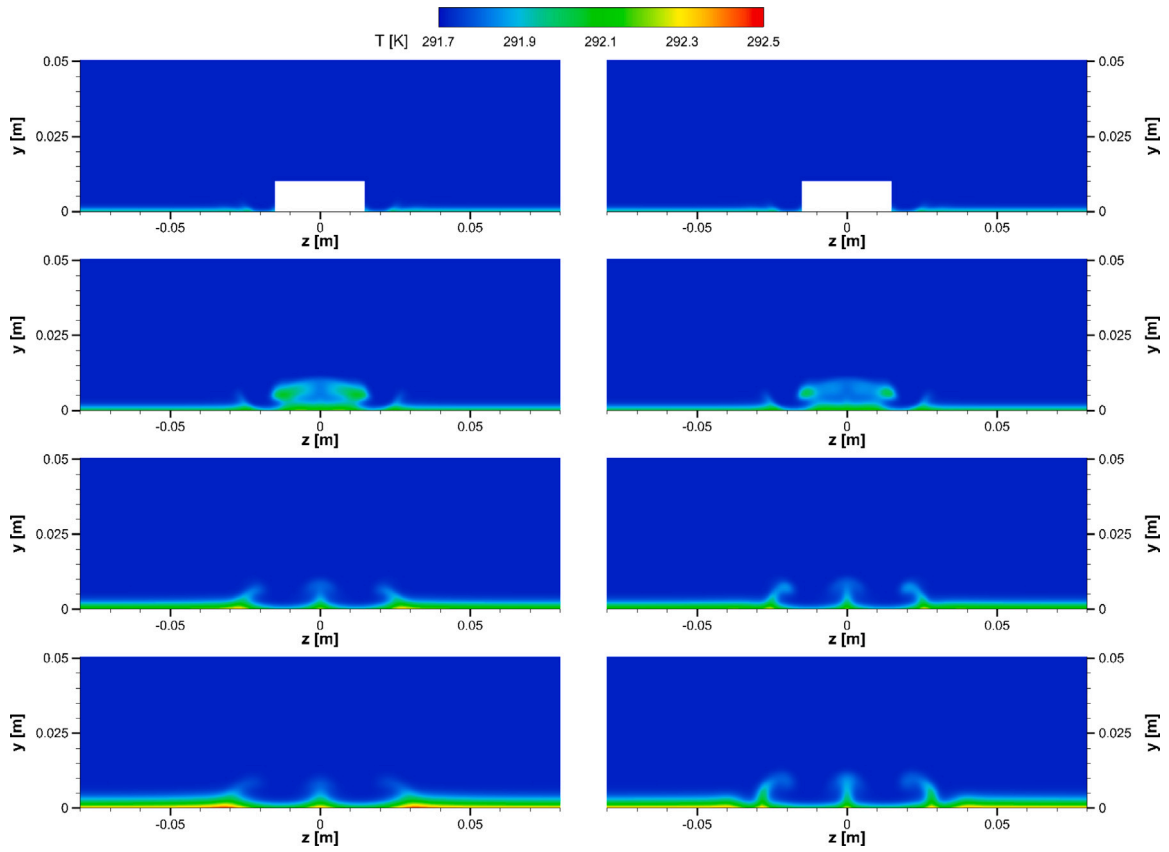

Fig. 15. Cross sectional view of the temperature at $x = 0\,\mathrm{m}$ ($x = x_k$), $0.03\,\mathrm{m}$ ($x/k = 1$), $0.15\,\mathrm{m}$ ($x/k = 5$), and $0.30\,\mathrm{m}$ ($x/k = 10$) from the center of the roughness element. The origin with $x = z = 0$ corresponds to the center position of the roughness element. The left and right columns show results for simulations excluding and including buoyancy effects, respectively.

4. Summary

This study compared experimental and simulation results of a laminar boundary layer developing over a heated flat plate and the interaction of a laminar boundary layer with a single cylindrical roughness element of small aspect ratio. The experiments were performed in a water channel using temperature-sensitive paint and the simulations used the Fluent software package. Generally good agreement between the experiments and simulations was obtained with correlation coefficients of the temperature fields on the heated surface reaching values of 0.99 in the case of the laminar boundary layer and 0.95 in the more complex case of the interaction of the laminar boundary layer with the roughness element, provided that buoyancy effects are considered in the simulation.

The simulation results both provide more understanding of the experiments as well as extend the experimental observations. A first finding was the quantification of the losses occurring in electrical wiring and heat transfer away from the water region, which led to a decrease of the electrical heating power density effectively applied in the experiment. Since the best match between simulation and experiment was obtained for $100\,\mathrm{W/m^2}$, this loss could be estimated to be about $25\,\%$ of the electrical heating power density supplied by the power units.

A second finding was the identification of the role played by buoyancy effects in the formation of additional vortical structures in the presence of the roughness element, which led to the streamwise-oriented footprints on the heated wall observed in the experiment. In fact, the main flow topology (consisting of a horseshoe vortex wrapping around the roughness element, a recirculation zone in the near wake past the roughness element, and a trailing counter-rotating vortex pair stretching into the far wake) was observed in both simulations with and without buoyancy effects, but tertiary and further vortical structures were revealed by the simulation only with consideration of buoyancy effects. This complex system of counter-rotating vortex pairs was consistent with the surface temperature distribution measured in the experiment and with the topology reported in other work.

The present study also motivates future work. A variation of the heat flux density could lead to a better understanding of criteria to avoid thermal convection motions in experiments employing thermographic methods. Such a study might also provide insights into the structure of thermal convection motions potentially occurring at higher heat flux densities. Other directions for future work could include the consideration of in-plane conduction in the heated plate over which the boundary layer develops, an extension of the current study to higher Reynolds numbers with unsteady effects in the wake past the roughness elements, and the connection between the temperature on the heated wall and the wall shear stress could be quantified.

CRediT authorship contribution statement

Frank G. Jacobitz: Writing – review & editing, Writing – original draft, Visualization, Validation, Supervision, Software, Resources, Project administration, Methodology, Investigation, Formal analysis, Data curation, Conceptualization. **Ian Sysyn:** Visualization, Validation, Software, Formal analysis, Data curation. **Jacob Ryan:** Visualization, Validation, Software, Formal analysis, Data curation. **Jack Comfort:** Visualization, Validation, Software, Formal analysis, Data curation. **Patrick Bonner:** Visualization, Software, Investigation. **Dylan Poole:** Visualization, Software. **Jonathan Lemarechal:** Writing – review & editing, Writing – original draft, Visualization, Validation, Methodology, Investigation, Formal analysis, Data curation, Conceptualization. **Marco Costantini:** Writing – review & editing, Writing – original

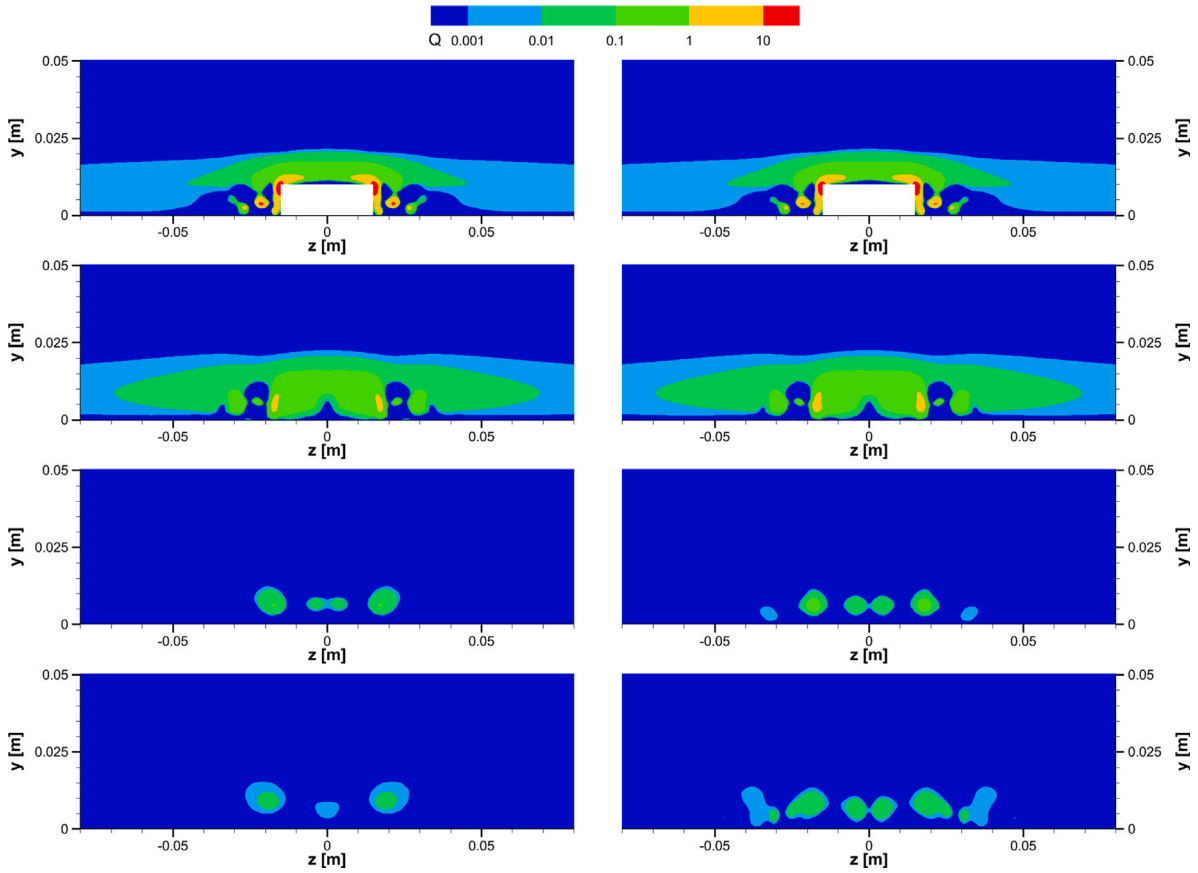

Fig. 16. Cross sectional view of the Q-criterion at $x = 0\,\mathrm{m}$ ($x = x_k$), $0.03\,\mathrm{m}$ ($x/k = 1$), $0.15\,\mathrm{m}$ ($x/k = 5$), and $0.30\,\mathrm{m}$ ($x/k = 10$) from the center of the roughness element. The origin with $x = z = 0$ corresponds to the center position of the roughness element. The left and right columns show results for simulations excluding and including buoyancy effects, respectively.

draft, Visualization, Validation, Supervision, Resources, Project administration, Methodology, Investigation, Formal analysis, Data curation, Conceptualization.

Declaration of competing interest

The authors declare that they have no known competing financial interests or personal relationships that could have appeared to influence the work reported in this paper.

Acknowledgments

FGJ acknowledges the travel support though an International Opportunity Grant from the University of San Diego and the hospitality at the DLR in Göttingen. The authors thank C. Klein (DLR) for the TSP application on the TSP element and for initiating this collaborative work between the University of San Diego and the DLR Göttingen. JL and MC acknowledge T. Kleindienst (DLR), C. Fuchs (DLR), V. Ondrus (FH Münster), E. Lagemann (University of Washington), and M. Weberschock (Weberschock Development) for the support during the design, manufacturing and development of the TSP element, and D. K. Puckert and U. Rist (University of Stuttgart) for the support to the design and conduction of the experiment in the laminar water channel. The authors acknowledge also the anonymous Reviewers for their comments, which motivated additional simulations that eventually elucidated the role played by buoyancy effects at the examined flow conditions.

Appendix A. Supplementary data

Supplementary material related to this article can be found online at https://doi.org/10.1016/j.ijheatfluidflow.2024.109656.

Data availability

Data will be made available on request.

References

Acarlar, M., Smith, C., 1987. A study of hairpin vortices in a laminar boundary layer. Part 1. Hairpin vortices generated by a hemisphere protuberance. J. Fluid Mech. 175, 1–41.

ANSYS, Inc, 2023. ANSYS fluent fluid simulation software. https://www.ansys.com/products/fluids/ansys-fluent.

Avallone, F., Schrijer, F., Cardone, G., 2016. Infrared thermography of transition due to isolated roughness elements in hypersonic flows. Phys. Fluids 28, 024106.

Bird, R., Stewart, W., Lightfoot, E., 2002. Transport Phenomena, 2nd ed. J. Wiley, New York, p. 318, 359.

Braslow, A., 1960. Review of the Effect of Distributed Surface Roughness on Boundary-Layer Transition. NASA TM-79879.

Braslow, A., 1966. A Review of Factors Affecting Boundary-Layer Transition. NASA TN D-3384.

Capone, A., Klein, C., Di Felice, F., Beifuß, U., Miozzi, M., 2015. Fast-response underwater TSP investigation of subcritical instabilities of a cylinder in crossflow. Exp. Fluids 56, 196.

Cattafesta, L., Liu, T., Sullivan, J.P., 1998. Uncertainty estimates for temperature-sensitive paint measurements with charge-coupled device cameras. AIAA J. 36, 2102–2108.

Chung, D., Hutchins, N., Schultz, M., Flack, K., 2021. Predicting the drag of rough surfaces. Annu. Rev. Fluid Mech. 53, 439–471.

Clark, J., Magari, P., Jones, T., 1993. On the distribution of the heat transfer coefficient in turbulent and "transitional" wedges. Int. J. Heat Fluid Flow 14, 217–222.

Costantini, M., Fey, U., Henne, U., Klein, C., 2015. Nonadiabatic surface effects on transition measurements using temperature-sensitive paints. AIAA J. 53, 1172–1187.

Costantini, M., Henne, U., Risius, S., Klein, C., 2021. A robust method for reliable transition detection in temperature-sensitive paint data. Aerosp. Sci. Technol. 113, 106702.

Egami, Y., Klein, C., Henne, U., Bruse, M., Ondrus, V., Beifuss, U., 2009. Development of a highly sensitive temperature-sensitive paint for measurements under ambient (0-60 °C) conditions. In: 47th AIAA Aerospace Sciences Meeting Including the New Horizons Forum and Aerospace Exposition, AIAA 2009-1075.

Ergin, F., White, E., 2006. Unsteady and transitional flows behind roughness elements. AIAA J. 44, 2504–2514.

Fey, U., Egami, Y., 2007. Transition detection by temperature-sensitive paint. In: Tropea, C., Yarin, A., Foss, J. (Eds.), Springer Handbook of Experimental Fluid Mechanics. Springer Berlin, Heidelberg, New York, pp. 537–552.

Fey, U., Engler, R., Egami, Y., Iijima, Y., Asai, K., Jansen, U., Quest, J., 2003. Transition detection by temperature sensitive paint at cryogenic temperatures in the European Transonic Wind tunnel (ETW). In: ICIASF'03. IEEE, pp. 77–88.

Fey, U., Klein, C., Möller, T., Pöttner, J., Radespiel, R., Ondrus, V., Beifuß, U., 2013. Investigation of circular cylinder flow in water using temperature-sensitive paint. In: Dillmann, A., Heller, G., Kreplin, H.P., Nitsche, W., Peltzer, I. (Eds.), New Results in Numerical and Experimental Fluid Mechanics VIII. Springer Berlin Heidelberg, pp. 657–664.

Gregory, N., Walker, W., 1956. The Effect on Transition of Isolated Surface Excrescences in the Boundary Layer. ARC R. & M. No. 2779.

Klanfer, L., Owen, P., 1953. The Effect of Isolated Roughness on Boundary Layer Transition. RAE Tech. Memo. 355.

Klebanoff, P., Cleveland, W., Tidstrom, K., 1992. On the evolution of a turbulent boundary layer induced by a three-dimensional roughness element. J. Fluid Mech. 237, 101–187.

Klebanoff, P., Schubauer, G., Tidstrom, K., 1955. Measurements of the effect of two-dimensional and three-dimensional roughness elements on boundary-layer transition. J. Aeronaut. Sci. 22, 803–804.

Klein, C., Engler, R., Henne, U., Sachs, W., 2005. Application of pressure-sensitive paint for determination of the pressure field and calculation of the forces and moments of models in a wind tunnel. Exp. Fluids 39, 475–483.

Lemarechal, J., Costantini, M., Klein, C., Kloker, M., Würz, W., Kurz, H., Streit, T., Schaber, S., 2019a. Investigation of stationary-crossflow-instability induced transition with the temperature-sensitive paint method. Exp. Therm. Fluid Sci. 109, 109848.

Lemarechal, J., Klein, C., Puckert, D., Rist, U., 2021. Application of the temperature-sensitive paint method for quantitative measurements in water. Meas. Sci. Technol. 32, 105301.

Lemarechal, J., Klein, C., Ulrich, H., Puckert, D., Rist, U., 2019b. Detection of Lambda- and Omega-vortices with the temperature-sensitive paint method in the late stage of controlled laminar–turbulent transition. Exp. Fluids 60, 91.

Lemarechal, J., Mäteling, E., Klein, C., Puckert, D., Rist, U., 2018. Reattaching flow behind a forward-backward facing step investigated with temperature-sensitive paint. In: Dillmann, A., Heller, G., Krämer, E., Wagner, C., Bansmer, S., Radespiel, R., R. Semaan, R. (Eds.), New Results in Numerical and Experimental Fluid Mechanics XI. Springer International Publishing, Cham, pp. 285–293.

Lemarechal, J., Mäteling, E., Klein, C., Puckert, D., Rist, U., 2020. Visualization of near-wall structures of an isolated cylindrical roughness element in a laminar boundary layer without pressure gradient. In: Dillmann, A., Heller, G., Krämer, E., Wagner, C., Tropea, C., Jakirlić, S. (Eds.), New Results in Numerical and Experimental Fluid Mechanics XII. Springer International Publishing, Cham, pp. 674–683.

Liu, T., Campbell, B., Sullivan, J.P., 1995. Accuracy of temperature-sensitive fluorescent paint for heat transfer measurements. In: 30th Thermophysics Conference, AIAA 1995-2042.

Liu, T., Sullivan, J.P., Asai, K., Klein, C., Egami, Y., 2021. Pressure and Temperature Sensitive Paints, 2nd ed. Springer, Cham.

Mäteling, E., Lemarechal, J., Klein, C., Puckert, D., Rist, U., 2020. Experimental investigation of mixed convection in horizontal channel flow in combination with cylindrical roughness elements. In: Dillmann, A., Heller, G., Krämer, E., Wagner, C., Tropea, C., Jakirlić, S. (Eds.), New Results in Numerical and Experimental Fluid Mechanics XII. Springer International Publishing, Cham, pp. 533–542.

Miller, C., Tang, W., Sluder, E., Finney, M., McAllister, S., Forthofer, J., Gollner, M., 2018. Boundary layer instabilities in mixed convection and diffusion flames with an unheated starting length. Int. J. Heat Mass Transfer 118, 1243–1256.

Miozzi, M., Capone, A., Costantini, M., Fratto, L., Klein, C., Di Felice, F., 2019. Skin friction and coherent structures within a laminar separation bubble. Exp. Fluids 60, 13.

Miozzi, M., Capone, A., Di Felice, F., Klein, C., Liu, T., 2016. Global and local skin friction diagnostics from TSP surface patterns on an underwater cylinder in crossflow. Phys. Fluids 28, 124101.

Miozzi, M., Costantini, M., 2021. Temperature and skin-friction maps on a lifting hydrofoil in a propeller wake. Meas. Sci. Technol. 32, 114007.

Miozzi, M., Schröder, A., Schanz, D., Willert, C., Klein, C., Lemarechal, J., 2024. Skin-friction from temperature and velocity data around a wall-mounted cube. Exp. Fluids 65, 156.

Morton, C., Martinuzzi, R.J., Kindree, M., Shahroodi, M., Saeedi, M., 2018. Wake dynamics of a cantilevered circular cylinder of aspect ratio 4. Int. J. Heat Fluid Flow 72, 109–122.

Ondrus, V., Meier, R., Klein, C., Henne, U., Schäferling, M., Beifuß, U., 2015. Europium 1,3-di(thienyl)propane-1,3-diones with outstanding properties for temperature sensing. Sensors Actuators A 233, 434–441.

Plogmann, B., Würz, W., Krämer, E., 2014. On the disturbance evolution downstream of a cylindrical roughness element. J. Fluid Mech. 758, 238–286.

Puckert, D., Dieterle, M., Rist, U., 2017. Reduction of freestream turbulence at low velocities. Exp. Fluids 58, 45.

Schröder, A., Willert, C., Schanz, D., Geisler, R., Jahn, T., Gallas, Q., Leclaire, B., 2020. The flow around a surface mounted cube: a characterization by time-resolved PIV, 3D Shake-The-Box and LBM simulation. Exp. Fluids 61, 189.

Smith, A., Clutter, D., 1959. The smallest height of roughness capable of affecting boundary-layer transition. J. Aerosp. Sci. 26, 229–245.

Strunz, M., Speth, J., 1987. A new laminar water tunnel to study the transition process in a Blasius boundary layer and in a separation bubble and a new tool for industrial aerodynamics and hydrodynamic research. In: AGARD CP-413. pp. 25–1–25–5.

Sumner, D., Heseltine, J., Dansereau, O., 2004. Wake structure of a finite circular cylinder of small aspect ratio. Exp. Fluids 37, 720–730.

Tani, I., Komoda, H., Komatsu, Y., Iuchi, M., 1962. Boundary-layer transition by isolated roughness. Report No. 375, Aeronautical Research Institute, University of Tokyo.

White, E., Reshotko, E., 2002. Roughness-induced transient growth in a flat-plate boundary layer. In: 40th AIAA Aerospace Sciences Meeting & Exhibit, AIAA 2002-0138.

Wiegand, T., 1996. Experimentelle Untersuchung zum laminar-turbulenten Transitionsprozeßeines Wellenzuges in einer Plattengrenzschicht (Ph.D. thesis). University of Stuttgart.

Ye, Q., Schrijer, F., Scarano, F., 2016. Geometry effect of isolated roughness on boundary layer transition investigated by tomographic PIV. Int. J. Heat Fluid Flow 61, 31–44.

Zhong, S., Chong, T., Hodson, H., 2003. A comparison of spreading angles of turbulent wedges in velocity and thermal boundary layers. J. Fluids Eng. 125, 267–274.

Zoppini, G., Ragni, D., Kotsonis, M., 2022. Transition due to isolated roughness in a swept wing boundary layer. Phys. Fluids 34, 084113.